

33 Severe Acute Respiratory Syndrome 2 (SARS-CoV-2) virus is responsible for Coronavirus disease 2019
34 (COVID-19) in over 144 million people and 3.0 million deaths as of April 22th 2021[1, 2]. The Spike(S)
35 glycoprotein studs the surface of Coronaviruses virions and its receptor-binding domain (RBD) binds host
36 cell receptors to mediate viral entry and infection[3, 4]. Greater than 90% of COVID-19 patients produce
37 neutralizing antibodies (nAbs)[5] and RBD-directed antibodies often comprise 90% of the total
38 neutralizing response[6]. RBD-directed antibodies can correlate with neutralizing activity[7-9] and ~2,500
39 antibodies targeting the SARS-CoV-2 spike have been described to date[10, 11]. This highlights the
40 importance of eliciting neutralizing antibodies targeting the RBD by vaccination.

41
42 Rational SARS-CoV-2 vaccine design should be informed by spike protein conformation dynamics, the sites
43 of vulnerability and mutations that cause potential vaccine escape. The S trimer has >3,000 residues
44 creating a vast array of epitopes and is targeted by both neutralizing and non-neutralizing antibodies(non-
45 nAbs)[12-15]. Measures of RBD binding do not always correlate with neutralization due to presence of
46 non-nAbs, which have the potential to cause antibody-dependent enhancement[16-18]. In the context of
47 HIV, influenza and MERS-CoV, significant effort over the last few decades has focused on creating
48 immunogens that minimize non-neutralizing epitopes[19-26]. Since the initial outbreak of SARS-CoV-2,
49 significant headway has been made in identifying neutralizing epitopes, especially with regards to the
50 RBD; however, study of immunodominant, non-neutralizing epitopes has lagged[14, 27, 28]. Vaccine
51 immunogens should be developed with these key findings in mind.

52
53 Glycosylation is an important post-translational modification in viral pathogenesis serving versatile roles
54 including host cell trafficking and viral protein folding[29]. Mutations introducing potential N-linked
55 glycosylation sites (PNGS) [30] in other viruses such as HIV and influenza have contributed to immune
56 escape[31-34]. Structure-based vaccine design efforts have been employed to add exogenous PNGS to
57 block non-neutralizing sites and focus the immune response to neutralizing sites[20, 26, 35, 36]. These
58 approaches have not been widely applied to SARS-CoV-2 vaccine development. Here, we develop an
59 advanced structural algorithm for optimizing PNGS into the SARS-CoV-2 RBD to focus the immune
60 response and enhance neutralizing responses targeting the Receptor Binding Site epitope(RBS).

61
62 Vaccine potency is important for an effective immunological response. Self-assembling, multivalent
63 nanoparticle immunogens (or nanovaccines) enhance the B cell activation and concomitant humoral
64 responses, kinetics of trafficking to the draining lymph nodes and uptake by dendritic cells and

65 macrophages[37-40]. SARS-CoV-2 nanovaccines developed as recombinant proteins can be difficult to
66 clinically translate due to arduous purification and manufacturing processes, and further do not tend to
67 activate CD8+ T cells[38]. In contrast, vaccine antigens encoded into a DNA plasmid can be delivered
68 directly *in vivo*. We recently demonstrated the speed of DNA vaccine translation by developing a DNA-
69 encoded full-length spike immunogen for clinical evaluation in 10 weeks[41]. DNA is easily mass produced,
70 temperature stable, not associated with anti-vector immunity and can be rapidly reformulated for
71 circulating variants, making it a key pandemic vaccine technology. We recently developed a DNA-launched
72 nanoparticle platform (DLNP) for *in vivo* assembly of nanoparticles which drive rapid and strong B cell
73 immunity and uniquely produce strong CD8+ T cells[38]. Here, we present a SARS-CoV-2 DLNP which has
74 enhanced immunity in multiple animal models and is capable of single shot protection against lethal
75 challenge. The single shot, low dose regimen reduces the overall amount of necessary product, medical
76 personnel, and time in the clinic, rendering the product more scalable to a global scope including resource
77 limited settings. The high potency and rapid developability of the DLNP platform can also enable quick
78 generation of booster vaccines for newly emergent variants. To this end, we developed a SARS-CoV-2
79 DLNP encoding P.1 mutations and demonstrate it is highly immunogenic.

80

81 **Results**

82 **Mapping antigenic effects of N-linked glycans on the RBD** To assess the feasibility of adding N-linked
83 glycans to alter antibody responses to RBD (Figure 1A), we built an advanced structural algorithm called
84 Cloaking With Glycans (CWG) for modeling every possible glycan on the RBD (Figure 1B). The PNGS
85 positions were filtered if the asparagine had low solvent accessibility or high clash score (Figure 1C). Next,
86 we surveyed energetics of naturally occurring glycans (Figure S1A, S1B) and employed glycan energy filters
87 for our designed glycan positions, as well as filters for protein folding energies and structural
88 considerations (see methods). This process led to the identification of 43 out of 196 positions for
89 experimental characterization (Figure 1C,1D).

90 To better understand single glycan mutants (Figure 2A), we produced each variant and measured
91 biophysical and antigenic profiles. We synthesized and screened the glycan variants for expression and
92 binding to ACE2 in a high-throughput, small-scale transfection format and downselected to 22 variants for
93 further evaluation (Figure 2B). To characterize the antigenic properties of the glycan variants, we utilized
94 14 RBD-directed nAbs, 2 Abs with inconsistent neutralization[42-45], and 6 non-nAbs[10, 12, 13, 15, 44-
95 51]. Most nAbs target epitopes in the RBS (RBD-A, RBD-B, RBD-C)[10] and some target outside the RBS[27]
96 (RBD-D, RBD-E and RBD-F) (Figure 2C). In general, we sought to identify glycans that do not interfere with

97 nAb binding and block non-nAbs. The reactivity of our set of antibodies to each glycan mutant was
98 determined by SPR and ELISA (Figure 2D,2E, Table S1). We observed reduced binding of neutralizing RBD-
99 A, RBD-B, RBD-C or RBD-D antibodies in the presence of glycans at residues 441, 448, 450, 458 and 481,
100 suggesting these could be potential vaccine escape mutations because they still bind human ACE2. In
101 addition, glycans at positions 337, 344, 354, 357, 360, 369, 383, 448, 450, 516 and 521 show dramatically
102 reduced binding to non-nAb(s). We did not observe effects on binding to our antibody panel for glycans
103 at 518, 519 and 520. We noticed similar antigenic patterns in glycan positions that reduce binding to
104 some of the non-nAbs as well as nAbs in RBS-E and RBS-F, suggesting there is overlap in these nAb and
105 non-nAb epitopes. In sum, our experimental screening exhaustively evaluated the effect of N-linked
106 glycans on the expression and antigenic profile of the RBD.

107
108 **N-linked glycan decoration improves RBD directed immunity** We utilized our single glycan data to add
109 sets of glycans to the RBD that maximally cover multiple non-neutralizing epitopes and preserve
110 accessibility to RBS targeted neutralizing epitopes. To this end, we constructed a glycan distance map
111 allowing design of three, five and eight glycan combinations which were experimental tested to
112 determine if the sets could provide optimized antigenic profiles (Figure 3A, S2A, S2B, S2C). Two of the
113 three glycan variants (g3.1 and g3.3) had heavily reduced binding to all antibodies in our panel. Eight
114 glycan variants (g8.1, g8.2 and g8.3) had slightly reduced EC_{50} to nearly all the RBD neutralizing
115 antibodies (Figure 3B). However, both g3.2 and g5.1 (harboring three and five glycans, respectively)
116 bound well to nAbs and had reduced affinity for non-nAbs (Figure 3B). Since new non-nAbs may be
117 identified in the future, we focused the remaining experiments on the more glycosylated variants (i.e.
118 g5.1 over g3.2), since they are more likely to reduce accessibility to epitopes recognized by non-nAbs.
119 We observed similar immunogenicity from BALB/c mice immunized with wild-type (WT) RBD or g5.1
120 RBD (Figure 3C,3D). To investigate the difference in specificity of the RBD elicited responses, we
121 employed an ACE2 blocking assay[52] (Figure 3E). We observed that RBD g5.1 elicited significantly more
122 ACE2-blocking antibodies than WT RBD, suggesting g5.1 is immune focusing antibodies to the RBS
123 (Figure 3F, 3G). This data demonstrates that combinations of strategically selected glycans reduce the
124 affinity of non-nAbs and focus immune responses to the neutralization-rich RBS or other epitopes of
125 interest.

126
127 **DNA-Launched nanovaccines amplify and accelerate immune responses** To develop multivalent
128 vaccines, we genetically fused RBDs to a set of four different self-assembling scaffold proteins[38-40,

129 53] with a potent CD4-helper epitope(LS-3) to help enhance germinal center responses[54]. Tandem
130 repeats of RBD have been shown to improve neutralization titers by 10-100 fold [55], thus we displayed
131 dimers of RBDs on some of our self-assembling scaffolds as well. We engineered nanoparticles using
132 our computational design methods[38], resulting in display of 7, 14, 24, 48, 60, 120 or 180 RBDs (Figure
133 4A). We rapidly screened 19 nanoparticles directly *in vivo* using a single mouse per construct at a single
134 low dose of 2 μ g. We observed that 14 of the 19 nanoparticles were immunogenic (Figure 4B). Strikingly,
135 rapid antibody responses were detected just 1 week after immunization with RBD g5.1 24mer, RBD
136 48mer and RBD g5.1 120mer (Figure 4B). In parallel, we expressed and purified nanoparticles *in vitro*.
137 In contrast to wild type RBD multimers, which we could not purify and were not more immunogenic
138 than RBD monomer (Figure S3A,S3B), we were able to purify nine glycan modified RBD multimers as
139 assessed by size exclusion chromatography with multiangle light scattering (Figure 4B,4C). To further
140 confirm assembly of the RBD g5.1 24mer, we employed structural analysis by cryo electron microscopy
141 (cryo-EM) for RBD g5.1 24mer (Figure 4D, 4E). We conducted immunizations with selected constructs
142 in BALB/c mice (n=5 or n=10) using a single low dose of 2 μ g (Figure 4F). RBD g5.1 24mer and 120mer
143 both generated strong binding and neutralizing responses (mean ID₅₀ of 3677 and 791, respectively)
144 (Figure S3C). In C57BL/6 mice, we observed similar immunogenicity at 1 μ g and 5 μ g doses for select
145 nanoparticles including improvements in CD8+ T cells (Figure S4A-S4E). RBD g8.2 7mer and RBD g8.2
146 24mer elicit similarly strong humoral responses when administered as purified protein nanoparticles
147 (Figure S5). Strikingly, we observed strong binding and neutralizing responses in BALB/c mice
148 immunized with 5 μ g RBD g5.1 24mer against the emergent South Africa (B.1.351), UK (B.1.17) and the
149 Brazilian variant (P.1), indicating cross-reactivity and strong potential relevance against emerging
150 variants (Figure 4G, S6A). As proof-of-concept for expanding this platform to emerging variants, we
151 engineered P.1 RBD g5.1 24mers. Upon of BALB/c mice immunization with 2 μ g, we observed high
152 binding and cross-neutralization titers (Figure 4H, 4I, S6B).

153
154 **Single dose of RBD nanoparticles affords protection in lethal challenge model** To examine the efficacy
155 of the SARS-CoV-2 RBD nanoparticles with rapid seroconversion(RBD g5.1 24mer and RBD g5.1 120mer),
156 we pursued a lethal challenge study (Figure 5A). B6.Cg-Tg(K18-ACE2)2PrImn/J(K18-hACE2) mice express
157 human ACE2 on epithelial cells including in the airway[56, 57] and can be infected with SARS-CoV-2
158 resulting in weight loss and lethality[58] providing a stringent model for testing vaccines[59]. Animals
159 were vaccinated with a single shot of 5 μ g and 1 μ g of our nanovaccines in K18-ACE2 mice representing
160 doses 5- and 25-fold lower than our standard DNA dose[41]. Prior to a blinded challenge, we examined

161 immunogenicity at day 21 and observed pseudovirus neutralization titers prior to challenge in all vaccine
162 groups (Figure S7). We also observed live SARS-CoV-2 virus neutralization titers above the limit of
163 detection for all three nanoparticle groups with mean ID₅₀ of 451, 1028, and 921 for RBD g5.1 120mer
164 1µg, 5µg and RBD g5.1 24mer 5µg, respectively, compared to a mean ID₅₀ of 29 of RBD monomer (Figure
165 5B). The mice were infected with SARS-CoV-2 1x10⁵ PFU/mouse intranasally and monitored for signs of
166 deteriorating health. We observed that mice immunized with nanovaccines had higher levels of protection
167 from weight loss (Figure 5C). As expected, the naive group of animals reached 100% morbidity by day 6
168 and 1/10 animals survived in the RBD monomer group. In both RBD g5.1 120mer groups had 6/10 mice
169 survived the challenge. Strikingly, immunization with RBD g5.1 24mer provided full protection from a
170 lethal SARS-CoV-2 challenge (Figure 5D). All but one animal that survived had a live virus neutralization
171 titer of >100 and 12/15 of the mice that succumbed to infection did not have appreciable neutralization
172 titers (Figure 5E). We observed a significant correlation between live virus neutralization ID₅₀ titer and
173 body weight loss (Figure 5F). Viral replication was reduced in nasal turbinates, lung tissue and brain tissue
174 for mice immunized with nanovaccines relative to RBD monomer or naïve animals (Figure 5G). Thus, the
175 DNA-launched nanovaccines can generate potent immunity that provides protection from challenge with
176 a single immunization at a low dose.

177
178 **Enhanced immune responses to nanovaccines in translational vaccine models** One major challenge for
179 the clinical translation of vaccines is preclinical modeling of human antibody responses to immunogens.
180 OmniMouse[®] have humanized immunoglobulin loci-transgenic with human V, D and J gene segments[60].
181 As a proof-of-concept, we immunized OmniMouse[®](n=3) with three different SARS-CoV-2 nanoparticle
182 vaccines and measured increasing RBD-specific human antibodies in serum (Figure 6A,6B). Most mice
183 produced high titers of IgG and a few had robust IgM titers (Figure S8A,S8B). We observed potent and
184 specific neutralization in all three groups at weeks 6 and 8 (Figure 6C, S8C). Thus, the SARS-CoV-2
185 nanoparticle platform can be employed in transgenic mice and induce human SARS-CoV-2 neutralizing
186 antibodies.

187 We assessed RBD g5.1 24mer in Hartley guinea pigs (n=6) to examine intradermal vaccine delivery at 0.5,
188 5 and 10µg in comparison to RBD monomer at 10µg. In contrast to the RBD monomer immunized group,
189 we observed full seroconversion of RBD g5.1 24mer immunized animals at a dose of 5µg (Figure 6D). High
190 levels of neutralizing antibodies were obtained in the 10µg dose group (ID₅₀ of 1840) (Figure 6E). In a
191 proof-of-concept study of RBD DLNPs prior to the development of RBD g5.1 24mer, we immunized Syrian
192 Golden hamsters (n=5) twice 3 weeks apart with 2µg and 10 µg of RBD monomer and RBD 48mer (Figure

193 6F). The RBD nanoparticle immunized hamsters elicited higher antibody titers after both first and second
194 doses and produced neutralizing antibodies unlike the responses in the RBD monomer vaccine groups
195 (Figure 6G). To assess the biodistribution of anti-RBD IgG, we measured ultrafiltrated lung lavages and
196 found antibodies only in the RBD nanoparticle groups (Figure 6H). In summary, we demonstrate that the
197 DLNP vaccines provide enhanced immunogenicity in guinea pigs and hamsters.

198

199 **Discussion**

200 New SARS-CoV-2 vaccines should (1) alleviate cold chain requirements for global vaccine distribution, (2)
201 improve immunogenicity for certain populations, (3) increase efficacy with a single dose and (4) protect
202 against emerging variants that reduce or evade current vaccine-induced immunity. We have
203 demonstrated that advanced DNA formulation and delivery technology coupled with immune focused
204 nanovaccines can provide a platform to address these translational obstacles for SARS-CoV-2 vaccines.

205 Viral glycan evolution results in antigenic changes with concomitant immune evasion. It has been
206 observed that for influenza, humoral immunity becomes restricted over time due to glycan additions[61].
207 SARS-CoV-2 mutational variants may escape from antibody-mediated immunity. Glycan mutational
208 variants may begin to circulate given their large impact on antibody recognition of virus. Here, we provide
209 a map of possible glycan additions to the RBD of SARS-CoV-2 and their effect on a large series nAbs.
210 Interestingly, we find a glycan at position 458, 369, 450 and 441 can bind to human ACE2, but strongly
211 reduces binding to nAbs targeting the sites RBD-A, B, C and D respectively. We also show that addition of
212 glycans to RBD-based nanovaccines can improve expression, assembly and immunogenicity.

213 The synthetic DNA platform employed in this study can be leveraged for generation of enhanced
214 immunity, easier global distribution and rapid reformulation. New adaptive electroporation systems can
215 improve uptake of DNA plasmid by 500x[62]. In stark contrast to complex recombinant protein and RNA-
216 based product development, DNA-based production and purification are extremely easy due to
217 availability of off the shelf commercial purification kits used widely in research laboratories. DNA vaccines
218 are also much more chemically and thermally stable allowing storage at room temperature for long
219 periods of time. These characteristics of the DNA platform allows for new vaccines to be developed at
220 breakneck speed and distributed to resource limited settings around the globe.

221 A key finding in this study is the dose-sparing immunogenicity afforded by the nanoparticle designs. Most
222 SARS-CoV-2 vaccines require at least two doses[63, 64]. DNA vaccines often require higher vaccine doses
223 (25 μg in mice[41] and 5 mg in NHPs[65]) and/or advanced delivery devices to drive sufficient
224 immunogenicity. Here, we observed strong immunogenicity and protection from bona fide SARS-CoV-2
225 challenge down to 1 μg . However, we did observe weight loss in 2/6 mice after challenge and low viral
226 titers in 2/4 mice sacrificed four days after challenge. Increasing the dose to 10 μg or by prime-boosting
227 could improve on our results. In fact, our studies of DNA-launched nanoparticle vaccines in guinea pigs
228 and hamsters demonstrated greater immunogenicity than RBD monomer at a low dose of 10 μg .

229 In comparison to other RBD nanoparticle systems, we have demonstrated significant improvements.
230 Recently, studies on two-component spike-based nanoparticle showed strong immunogenicity with
231 sporadic pseudovirus neutralization 2 weeks post prime[66, 67]. After 2 doses of the i53-50 RBD
232 nanoparticle vaccine, mice challenged with 1×10^5 PFU of a mouse-adapted non-lethal virus were observed
233 to have reduced viral replication[67]. SpyTag-coupled RBD nanoparticles induce binding but not
234 neutralizing antibodies 2-weeks post prime[68-71]. An RBD-HR SpyTag nanoparticle was observed to
235 induce immunity after 2 doses which after challenge with 4×10^4 PFU authentic SARS-CoV-2 could reduce
236 viral load in the lungs[72]. Here, the DNA-launched glycan modified RBDs could be genetically fused with
237 *four* different nanoparticles scaffolds, the simple genetic fusion results in a single vaccine product that
238 could induce binding and neutralizing antibodies 1 week post prime immunization and induce CD8+ T cells.
239 We created a more stringent test of immunity than most previous studies as we used authentic SARS-
240 CoV-2 virus with 2.5-fold higher amount of virus (1×10^5 PFU) in the challenge and a 10-fold more sensitive
241 viral detection assay. Further, vaccines studied in this model mostly utilize a prime and boost to achieve
242 protection (personal communication, Texas Biomed). In this model, our nanovaccines could induce
243 immunity that reduced viral replication and completely protected from death at a low single dose of 5 μg .
244 From the data, there is an 82% chance of survival if mice have a live virus neutralization titer >100 prior
245 to challenge. Given the protective threshold for neutralizing antibodies that we observe, we expect that
246 the high levels of cross-reactivity neutralization to the B.1.1.7, B.1.351, P.1 SARS-CoV-2 variants generated
247 by our nanovaccine would protect in a similar lethal challenge. In addition, the P.1 RBD g5.1 nanoparticle
248 elicited high levels of cross-reactive antibodies which could be employed as a booster vaccine.

249 In conclusion, we have developed single-dose SARS-CoV-2 nanovaccine with a platform that can afford
250 rapid pre-clinical reconfiguration to address variants of concern and for clinical translation.

251 **Methods**

252

253 **Cloaking with Glycans Algorithm**

254 The modeling started with RBD structure PDB id: 6M0J. GlycanTreeModeler(GTM) is a glycan modeling
255 algorithm recently developed in Rosetta(unpublished). The Cloaking With Gycans (CWG) workflow utilizes
256 GTM for selecting single glycan addition positions on target protein. All steps in CWG are summarized in
257 a flowchart (Figure 1B). CWG begins with detecting native sequons and modeling all the native glycan
258 structures using Man9GlcNAc2 glycans on the target protein. In the next stage, a model is made for the
259 addition of a single glycan at each position. A given position in the protein is mutated to asparagine and
260 the i+2 position is mutated into threonine or serine. The model with the lowest energy i+2 position is used
261 for further evaluation. The Rosetta energy is computed for the resulting model. We filtered out positions
262 if the total energy of the model corresponding to that position had a total energy > 5 Rosetta Energy Units
263 (REU) more than the native structure. Next, the CWG algorithm builds Man9GlcNAc2 glycans on the
264 mutated position and measures repulsive energy of engineered glycan between sugar-sugar and sugar-
265 protein energy terms. We filtered out some positions based on structural criteria, such as avoiding the
266 mutation of positions involved in disulfide bonds. Man9GlcNAc2 glycans were utilized for simplicity.

267

268 **Nanoparticle modeling**

269 All nanoparticles were modeled with corresponding designed structures and linkers. Four nanoparticles
270 were used in this study: IMX313P (PDB id: 4B0F), ferritin (PDB id: 3BVE), lumazine synthase (PDB id: 1HQK),
271 and PcV (PDB id: 3J3I). Biological unit nanoparticle structure files were downloaded in CIF format. The
272 termini of the monomeric RBDs were aligned to the termini of the nanoparticle, rotational and
273 translational degrees of freedom were sampled to reduce clashing between RBDs and nanoparticles,
274 extended linkers of various lengths were then aligned to fuse the nanoparticle and immunogen with
275 simpleNanoparticleModeling from the MSL library as previously described[38].

276

277 **Protein expression and purification**

278 Glycosylated RBDs: A gene encoding the amino acids 331-527 of the SARS-CoV-2 spike glycoprotein (PDB:
279 6M0J) was mutated at each position according to CWG. Nanoparticles were genetically fused to designed
280 RBDs as described above. DNA encoding the variants were codon optimized for homo sapiens and cloned
281 with a IgE secretion sequence into the pVAX vector. A 6xHisTag was added to the c-terminus of the RBD
282 monomer variants. ExpiF293 cells were transfected with the pVAX plasmid vector either carrying the

283 nanoparticles or the His-Tagged monomer transgene with PEI/Opti-MEM and harvested 6-7 days post
284 transfection. The supernatants was first purified with affinity chromatography using the AKTA pure 25
285 purification system and IMAC Nickel column (HisTrap™ HP prepacked Column ,Cytiva) for His-tagged
286 monomers and gravity flow columns filled with Agarose bound Galnthus Nivalis Lectin beads (Vector Labs)
287 for nanoparticles. The eluate fractions from the affinity chromatography were pooled, concentrated, and
288 dialyzed into 1X PBS before being loaded onto the Size-Exclusion Chromatography (SEC) column for
289 further purification with Superdex 200 Increase 10/300 GL column for the His-tagged monomers and the
290 Superose 6 Increases 10/300 GL column for the nanoparticles. Fractions of interest were pooled and
291 concentrated for characterization. For antibody production, heavy and light chains were encoded in
292 pFUSEss-CHlg-hG1, and pFUSE2ss-CLlg-hk or pFUSEss-CLlg-hL2 respectively and were co-transfected in
293 equal parts using ExpiFectamine™ 293 Transfection Kit(Gibco) according to manufacturer's protocol.
294 Antibodies were purified by affinity chromatography using the Protein A column (HiTrap™ MabSelect™
295 SuRe, Cytiva) and AKTA Pure 25 purification system.

296

297 **Western Blot**

298 Samples were prepared with 13 µL supernatants of Expi293F cells transfected with RBD monomer
299 plasmids or 0.65 µg of purified WT RBD in 1x PBS, NuPAGE LDS Sample Buffer (Novex), and NuPAGE
300 Sample Reducing Agent (Novex) were denatured at 90°C for 10 minutes. Samples were loaded in a 4-12%
301 SDS Bis-Tris gel for electrophoresis then transferred from the gel onto a PVDF membrane. The membrane
302 was blocked with Intercept (PBS) Blocking Buffer (LI-COR) for >1 hour at ambient temperature then
303 incubated with *** µg / protein gel of MonoRab anti-his tag C-term (Genscript) in Intercept T20 (PBS)
304 Antibody Diluent (LI-COR) overnight at 4°C. The membrane was then incubated in a 1:10000 IRDye 800CW
305 goat anti-rabbit IgG (LI-COR Biosciences) in Intercept T20 (PBS) Antibody Diluent (LI-COR) at room
306 temperature for 1 h. Membranes were imaged with a LI-COR Odyssey CLx.

307

308 **ELISA**

309 For in vitro characterization, high Binding, 96-well Flat-Bottom, Half-Area Microplate (Corning) were
310 coated at 1 µg/mL 6x-His tag polyclonal antibody (Invitrogen) for >4 hours at ambient temperature and
311 blocked ≥1 hour with 5% milk/1x PBS/0.01% Tween-20 at 4°C. RBD transfection supernatant or
312 recombinant protein at 10 µg /mL was incubated for 1-2 hours at ambient temperature. Serial dilutions
313 of antibodies were made according to affinity and incubated on plate for 1-2 hours at ambient
314 temperature. Goat anti-Human IgG-Fc fragment cross-adsorbed antibody HRP conjugated (Bethyl

315 Laboratories) secondary at a 1:10,000 dilution for 1 hour at ambient temperature. All dilutions except
316 coating were performed in 5% milk/1x PBS/0.01% Tween-20 and plates were washed with 1x PBS/0.05%
317 Tween-20 between steps. 1-Step™ Ultra TMB-ELISA Substrate Solution (Thermo Scientific) was incubated
318 on the plate for 10 minutes in the dark and then quenched with 1 M H₂SO₄. Absorbance of samples at
319 570 nm was subtracted from 450 nm for each well and background of blank wells were subtracted from
320 each well before analysis. Curves were analyzed in GraphPad Prism 8 with Sigmoidal, 4PL, X is
321 concentration and AUC.

322 For serology, plates were coated with 1 µg/mL 6x-His tag polyclonal antibody (Invitrogen) in 1x PBS for 6
323 hours at ambient temperature and blocked overnight with 0.5% NCS/5% Goat Serum/5% Milk/0.2% PBS-
324 T. 5x serial dilutions of sera were made starting at a 1:100 dilution and incubated on plate for 2 hours at
325 37 °C. For BL6, BALB/c, and K18 ACE2 mouse studies, goat anti-mouse IgG h+I HRP-tagged antibody (Bethyl
326 Laboratories) diluted 1:20000. For the OmniMouse® study, Peroxidase AffiniPure Goat Anti-Rat IgG
327 (Jackson ImmunoResearch) at 1:10000, Peroxidase AffiniPure F(ab')₂ Fragment Goat Anti-Rat IgM, µ chain
328 specific (Jackson ImmunoResearch) at 1:10000, Goat anti-Human Kappa Light Chain Antibody HRP
329 Conjugated (Bethyl Laboratories) at 1:10000, Goat anti-Human Lambda Light Chain Antibody HRP
330 Conjugated (Bethyl Laboratories) at 1:10000, and Goat anti-Mouse IgG-heavy and light chain Antibody
331 HRP Conjugated (Bethyl Laboratories) at 1:20000, and Goat anti-guinea pig IgG whole molecule (Sigma)
332 at 1:10,000 were used. Secondary antibodies were incubated on plates for 1 hr at RT. All dilutions except
333 coating were performed in 1% NCS in 0.2% PBS-T and plates were washed with 1x PBS/0.05% Tween-20
334 between steps. Plates were developed with 1 Step Ultra TMB substrate in the dark for 10 minutes for
335 mouse studies and 15 minutes for guinea pig studies before being quenched with 1N H₂SO₄ and read using
336 a BioTek Synergy 2 plate reader at an absorbance of 450 and 570nm.

337 Hamster serology was performed by directly coating 96-well flat bottom, half-area plates #3690 (Corning)
338 with 25mL of 1 µg /mL of SARS-CoV-2 RBD (University of Texas, Austin) overnight at 4°C. Plates were
339 blocked with 100uL of blocking buffer (3% BSA in 1 x PBS) for 1 hr at 37°C. Hamster sera was diluted to
340 1:16 dilution in diluent buffer (1% BSA in PBS) and an 11-point 1:3 serial dilution was done on the ELISA
341 plate, with last column containing only dilution buffer as blank control. ELISA plates were incubated for 2
342 hr at 37°C with sera dilutions. Anti-Hamster HRP antibody (Sigma) was diluted in diluent buffer 1:10,000
343 and were incubated for 1 hr at room temperature. SureBlue TMB 1-Component Microwell Peroxidase
344 Substrate (KPL) was added to the wells and plates were incubated for 6 minutes and then quenched with
345 TMB Stop Solution (KPL). Absorbance was immediately read at 450 nm on Synergy HTX plate reader

346 (BioTek). All volumes except blocking buffer was 25uL. Plates were washed 3 times with wash buffer (.05%
347 Tween 20 in 1x PBS) between steps.
348

349 **Surface Plasmon Resonance**

350 RBD-antibody kinetics experiments were performed with a Series S Sensor Protein A capture chip (Cytiva)
351 on a Biacore 8k instrument (GE). The running buffer was HBS-EP (3 M sodium chloride/200 mM HEPES/60
352 mM EDTA/1.0% Tween 20 pH=7.6) (Teknova) with 0.1% (w/v) bovine serum albumin. Each experiment
353 began with two start up cycles with 60 s of contact time and a flow rate of 50 μ L/min. For analysis
354 methods, approximately 200-300 RUs of IgG antibodies was captured on each flow cell at a flow rate of
355 10 μ L/min for 60 seconds. WT RBD or glycan variants samples were 5x serial diluted from 1000 nM in
356 running buffer and flowed across the chip after capture at a 50 μ L/min rate. The experiment had a
357 120 second contact time phase and 600 seconds dissociation phase. Regeneration was performed with 10
358 mM glycine at pH=1.5 at a flow rate of 50 μ L/min for 30 seconds after each cycle. Kinetic fits were analyzed
359 with 1:1 fitting and run through a script to filter out results that had poor fitting, low max RUs compared
360 to expected, and kon and koff constants that fell outside of the range of measurement. Experiments that
361 were flagged as poor-quality fitting by this script were not further analyzed.

362

363 **Pseudovirus Neutralization Assay**

364 HEK293T (CRL-3216) and CHO cells (CRL-12023: double check) were obtained from ATCC (Manassas, VA,
365 USA). Cells were maintained in DMEM supplemented with 10% fetal bovine serum (FBS) and 1% penicillin-
366 streptomycin (P/S) antibiotic at 37°C under 5% CO₂ atmosphere. For luciferase-based virus
367 pseudoneutralization assays, HEK293T cells were transfected to produce SARS-CoV-2 S containing
368 pseudoviruses. Cells were seeded at 5 million cells onto T75 flasks and grown for 24 hours. Then, cells
369 were treated with 48 μ L GeneJammer (Agilent 204130-21), 6 μ g S_IgE_deltaCterm19_plasmid (Genscript),
370 and 6 μ g pNL4-3.luc.R-E- backbone (Aldevron) and incubated for 48 hours. For variant pseudoviruses, cells
371 were similarly treated with GeneJammer and backbone with 6 μ g of S_SA_IgE_deltaCterm19,
372 S_UK_IgE_deltaCterm19, or S_Brazil_IgE_deltaCterm19 plasmid. Transfection supernatants were then
373 collected and supplemented with 12% FBS, sterile filtered, and stored at -80°C. Pseudovirus solutions
374 were titered and dilution to working solutions set such that they yielded >215-fold greater relative
375 luminescence units (RLS) than cells alone.

376 CHO cells expressing human ACE2 receptors (VCel-Wyb030) were obtained from Creative Biolabs (Shirley,
377 NY). CHO-ACE2 cells were seeded at 10,000 cells/well in 96-well plates and incubated for 24 hours. Sera
378 from vaccinated mice were heat inactivated at 56°C for 15 minutes. 3-fold serial dilutions starting at 1:20
379 dilutions in DMEM supplemented with 10% FBS and 1% P/S were performed on sample sera and incubated
380 for 90 minutes at room temperature with SARS-CoV2 pseudovirus based on concentrations determined
381 from titring described above. Media containing diluted sera and pseudovirus were then applied to CHO-
382 ACE2 cells. After 72 hours of incubation, cells were developed using BriteLite plus luminescence reporter
383 system (Perkin Elmer 6066769) and signal measured using a plate reader (Biotek Synergy). Percent
384 neutralization was calculated based on virus only positive control signal with background subtraction of
385 cells only negative controls. ID₅₀ values were calculated using GraphPad Prism v8.0 nonlinear curve fitting
386 with constraint Hill Slope < 0.

387

388 **SARS-CoV-2 culture, titer, and neutralization assay**

389 SARS-Related Coronavirus 2, Isolate USA-WA1/2020, NR-52281 was deposited by the Centers for Disease
390 Control and Prevention and obtained through BEI Resources, NIAID, NIH. All work with it was performed
391 in the BSL-3 facility at the Wistar Institute. Vero cells (ATCC CCL-81) were maintained in antibiotic-free
392 Dulbecco's modified Eagle's medium (DMEM) supplemented with 10% fetal bovine serum (FBS). To grow
393 a stock of virus, 3 million Vero cells were seeded in a T-75 flask for overnight incubation (37°C, 5% CO₂).
394 The cells were inoculated the next day with 0.01 MOI virus in DMEM. Culture supernatant was harvested
395 3 days post infection, aliquoted, and stored at -80°C. For titring the virus stock, Vero cells were seeded
396 in DMEM with 1% FBS at 20,000 cells/well in 96 well flat bottom plates for overnight incubation (37°C,
397 5% CO₂). The USA-WA1/2020 virus stock was serially diluted in DMEM with 1% FBS and transferred in
398 replicates of 8 to the previously seeded Vero cells. Five days post infection individual wells were scored
399 positive or negative for the presence of cytopathic effect (CPE) by examination under a light microscope.
400 The virus titer (TCID₅₀/ml) was calculated using the Reed-Munch method and the Microsoft Excel based
401 calculator published by Lei et al[73] For neutralization assays, Vero cells were seeded in DMEM with 1%
402 FBS at 20,000 cells/well in 96 well flat bottom plates for overnight incubation (37°C, 5% CO₂). Serum
403 samples were heat inactivated at 56°C for 30 minutes. Serum samples were then serially diluted in DMEM
404 with 1% FBS and 1% penicillin/streptomycin and incubated for one hour at room temperature with 300
405 TCID₅₀/ml USA-WA1/2020. The serum-virus mixture was then transferred in triplicate to the previously
406 seeded Vero cells. Five days post infection, individual wells were scored positive or negative for the

407 presence of CPE and neutralization titers were calculated using the Reed-Munch method and a modified
408 version of the Microsoft Excel based calculator published by Lei et al[73].

409

410 **Animal Studies**

411 C57BL/6, BALBc, and K18-hACE2 mice were obtained from Charles River Laboratories (Malvern, PA) and
412 The Jackson Laboratory (Bar Harbor, ME). Omni Mouse® for human antibody studies were obtained from
413 Ligand Pharmaceuticals Incorporated (San Diego, CA). All studies were performed in accordance with
414 Wistar Institutional Animal Care and Use Committees under approved animal protocols. All animals were
415 housed in the Wistar animal facility in ventilated cages and given free access to food and water. For the
416 lethal challenge study, Texas Biomed were blinded to identity of vaccination groups and weight loss cutoff
417 for euthanasia was 20%. Intramuscular injection with electroporation and sample collection. Plasmids
418 were administered intramuscularly in 30uL water into the tibialis anterior muscle. Electroporation was
419 then performed using CELLECTRA EP delivery platform consisting of two pulse sets at 0.2 Amps at a 3
420 second interval. Each pulse set consists of two 52 ms pulses with 198 ms delay. At specified time points,
421 blood was collected via submandibular vein puncture and centrifuged for 10 min at 15000 rpm to obtain
422 sera. For cellular responses, mice were euthanized under CO₂ overdose. Spleens were collected into cold
423 RPMI media supplemented with 10% FBS and 1% P/S.

424

425 Female Hartley guinea pigs (8 weeks old, Elm Hill Labs, Chelmsford MA) were housed at Acculab (San
426 Diego CA). On day 0 and day 28 animals were anaesthetized with isoflurane vapor and received
427 intradermal Mantoux injections of 100 µL 10, 5 or 0.5 µg pDNA immediately followed by CELLECTRA-3P
428 electroporation. The CELLECTRA® EP delivery consists of two sets of pulses with 0.2 Amp constant current.
429 Second pulse set is delayed 3 seconds. Within each set there are two 52 ms pulses with a 198 ms delay
430 between the pulses. Serum samples were collected by jugular or saphenous blood collection throughout
431 the study on days 0, 7, 14, 21, 28 and 42. Whole blood samples to process PBMCs for cellular assay were
432 collected from the jugular vein on days 14 and 42. All animals were housed in the animal facility at Acculab
433 Life Sciences (San Diego, CA). All animal protocols were approved by Acculab Institutional Animal Care
434 and Use Committees (IACUC).

435 Golden Syrian hamsters (8 weeks old, Envigo, Indianapolis, IN) were housed at Acculab (San Diego, CA).
436 Hamsters received intramuscular (IM) injections of 60 µL of 2 or 10µg pDNA formulation into the tibialis
437 anterior muscle immediately followed by electroporation with the CELLECTRA-3P device under Isoflurane
438 vapor anesthesia at day 0 and day 21. The CELLECTRA® EP delivery consists of two sets of pulses with 0.2

439 Amp constant current. Second pulse set is delayed 4 s. Within each set there are two 52 ms pulses with a
440 198 ms delay between the pulses. Serum samples were collected at indicated timepoints via saphenous
441 vein blood collection throughout the experiment. All animals were housed in the animal facility at Acculab
442 Life Sciences (San Diego, CA). All animal protocols were approved by Acculab Institutional Animal Care
443 and Use Committees.

444 In-vivo study was concluded with terminal blood, lung lavage and nasal wash collection. Lavage buffer was
445 prepared as PBS containing 100uM EDTA, 0.05% Sodium Azide, 0.05% Tween-20 and Protease Inhibitor.
446 Hamsters were euthanized by jugular exsanguination with intraperitoneal (IP) injection of 86.7mg/kg
447 pentobarbital sodium or overdose Isoflurane gas inhalation. Euthanized hamster was placed in supine
448 position and skin was disinfected using 70% Isopropyl alcohol. A longitudinal cut using scissors and blunt
449 dissection along the midline of the neck was performed to expose the trachea. An opening into the
450 exposed trachea was created by making a transverse, semilunar cut using #11 blade.

451 To collect nasal wash an 18ga blunt end needle was inserted toward the nose and gently proceeded
452 upwards until reaching the nasal palate. A syringe filled with 1.5mL lavage buffer was connected to the
453 blunt end needle and correct placement was tested by dispensing a small amount through the hamster's
454 nares. The entire volume of lavage fluid was rapidly dispensed and collected directly from the nares into
455 a 5.0mL Eppendorf tube.

456 To collect bronchioalveolar lavage (BAL), an 18ga blunt end needle, attached to a three-way stopcock and
457 primed with lavage buffer (approximately 0.5mL) to eliminate empty airspace, was inserted forward until
458 just prior to the tracheal bifurcation into the lungs. The blunt end needle was secured in the trachea with
459 a silk 2-0 tie. A 3mL receiver syringe and a 10mL syringe filled with 9mL of lavage buffer was connected
460 to the blunt end needle via the three-way stopcock. The lungs were rinsed three times (3mL each time)
461 with a total of 9mL lavage buffer. Typically, 50% of lavage buffer was recovered.

462

463 **Hamster biodistribution**

464 Lung lavage and nasal wash samples were ultrafiltrated using a 2mL 100kDa cut-off ultrafiltration device
465 (Millipore, Burlington MA) spinning 1mL BAL or NW for 15min at 4000g. Ultrafiltrated BAL was diluted 1:6
466 and nasal wash was diluted 1:4 in ELISA dilution buffer and following washes and blocking as described in
467 the ELISA section added to half area assay plates (Costar) coated with 25µL/well of 1 µg/mL SARS-CoV-2
468 RBD (Sinobiological) in dilution buffer overnight at 4C. BAL and NW samples were tested at a 7-step 1:2
469 serial dilution.

470

471

472 **Negative-stain electron microscopy**

473 Purified RBD g5.1 nanoparticle was dialyzed into 20 mM HEPES buffer, 0.15M NaCl, pH 7.4. A total of 3 μ L
474 of purified proteins was adsorbed onto glow discharged carbon-coated Cu400 EM grids. The grids were
475 then stained with 3 μ L of 2% uranyl acetate, blotted, and stained again with 3 μ L of the stain followed by
476 a final blot. Image collection and data processing was performed on a FEI Tecnai T12 microscope equipped
477 with Oneview Gatan camera at 90 450 \times magnification at the camera and a pixel size of 1.66 \AA .

478

479 **Cryo electron microscopy**

480 Cryo-EM vitrification was obtained in a Vitrobot Mark IV robot (FEI). Four μ L of purified RBD g5.1 24mer
481 nanoparticles in 1xPBS were deposited on a glow-discharged holey carbon grid (C-flat 1.2/1.3, 300 mesh;
482 Protochips). Excess liquid was blotted away followed by immediate plunging into liquid ethane cooled by
483 liquid nitrogen. The vitrified specimen was then introduced into an FEI Talos Arctica electron microscope
484 (FEI). Automated data collection was performed in EPU (FEI) and 640 movie micrographs were recorded
485 with a Falcon 3 camera (FEI) at 150,000 \times magnification corresponding to an image pixel size of 0.97 \AA on
486 the object scale. Each movie micrograph comprised 50 frames, each frame was exposed with a dose of ~ 1
487 $e^-/\text{\AA}^2$. Data processing was performed in Relion v3.1.2[74]. Movie micrograph frame alignment, spectral
488 signal weighing and summation was followed by CTF modeling (CTFFIND4[75]). Candidate molecular
489 projection images were identified with Relion LoG picking ($\sim 271,000$). Image windows corresponding to
490 the candidate molecular projection image coordinates were extracted and binned by a factor of 2. The
491 extracted binned data was subjected to 2D classification. Manual inspection of class averages led to
492 identification of 93,348 molecular projection images selected for further data processing. Molecular
493 projections were re-extracted unbinned from the summed micrographs and iterative Euler angular
494 reconstitution and 3D object reconstruction was performed with a low-resolution ferritin density map as
495 initial seed. 3D refinement was performed both asymmetrically (FSC 0.143 resolution 3.98 \AA) and under
496 the assumption of octahedral symmetry (FSC 0.143 resolution 3.42 \AA). Since our objective was to map the
497 attachment sites of the RBDs to the ferritin cage, we made no efforts to improve ferritin particle alignment
498 in our refinement strategy for the present manuscript.

499

500 **ELISpot assay**

501 Spleens from immunized mice were processed by a tissue stomacher, and red blood cells were then lysed
502 by ACK buffer (Thermo Fisher Scientific). Single cell suspension was counted, and 2×10^5 splenocytes were

503 plated into each well of the Mouse IFN- γ ELISpotPLUS plates (MabTech). The splenocytes were stimulated
504 for 20 hours at 37°C with RBD peptides (15-mer peptides overlapping by 9 amino acid spanning the RBD
505 of SARS-CoV-2 spike protein, GenScript), at 5 μ g/mL of each peptide in RPMI + 10% FBS (R10). The spots
506 were developed according to manufacturer's instructions. R10 and cell stimulation cocktails (Invitrogen)
507 were used for negative and positive controls, respectively. Spots were scanned and quantified by
508 ImmunoSpot CTL reader. Spot-forming unit (SFU) per million cells was calculated by subtracting the
509 negative control wells.

510

511 **Intracellular cytokine staining and Flow cytometry**

512 Splenocytes were processed as described in the previous section and stimulated with RBD peptides for 5
513 hours at 37°C with protein transport inhibitor (Invitrogen) and anti-mouse CD107a-FITC antibody
514 (BioLegend). Cell stimulation cocktail and R10, with protein transport inhibitor, were used as positive and
515 negative controls, respectively. After stimulation, cells were stained with Live/Dead violet (Invitrogen) for
516 viability. Anti-mouse CD4-BV510, CD8-APC-Cy7, CD44-A700, and CD62L-BV711 antibodies were used for
517 surface staining and CD3e-PE-Cy5, IFN- γ -APC, and TNF- α -BV605 (all from BioLegend) were used for
518 intracellular staining. The samples were run on an 18-color LSRII flow cytometer (BD Biosciences) and
519 analyzed by FlowJo software.

520

521 **Competition assay**

522 96-well Flat-Bottom Half-Area plates (Corning) were coated at room temperature for 8 hours with 1
523 μ g/mL 6x-His tag polyclonal antibody (PA1-983B, ThermoFisher), followed by overnight blocking with
524 blocking buffer containing 5% milk/1x PBS/0.01% Tween-20 at 4°C. The plates were then incubated with
525 RBD at 1 μ g/mL at room temperature for 1-2 hours. Mouse Sera (BALB/c ,terminal bleeds, week 6, n=5)
526 either immunized with RBD-WT or RBD-gPenta was serially diluted 3-fold starting at 1:20 with dilution
527 buffer (5% milk/1x PBS/0.01% Tween-20) was added to the plate and incubated at room temperature for
528 1-2 hours. Plates were then washed and incubated at room temperature for 1 hour with ACE2-IgHu at a
529 constant concentration of 0.06 μ g/mL diluted with the dilution buffer. After being washed, the plates were
530 further incubated at room temperature for 1 hour with goat-anti human IgG-Fc fragment cross-adsorbed
531 Ab (A80-340P; Bethyl Laboratories) at a 1: 10,000 dilution, followed by addition of TMB substrates
532 (ThermoFisher), and then quenched with 1M H₂SO₄. Absorbances at 450nm and 570nm were recorded
533 with a BioTek plate reader. Four washes were performed between every incubation step using PBS and
534 0.05% Tween-20. The assay was performed in triplicates. The average absorbance of the lowest dilutions

535 with saturating ACE2 signals was calculated to get a maximum ACE2 binding and no blocking. Each average
536 absorbance value was subtracted from the maximum to get an ACE2 blocking curve. The blocking titer is
537 defined as the reciprocal of the highest dilution where two consecutive dilutions have readings below
538 zero. The maximum area under the curve is determined by calculating the Area Under the Curve (AUC) of
539 full ACE2 binding without the competitor. The AUC of the competitor is then subtracted from the
540 maximum AUC which provides the area between the two curves (blocking area) and is a measure of ACE2
541 blocking. The fraction ACE2 blocking is defined as the fraction of the blocking area to the maximum AUC.
542

543 **Figure Legends**

544 **Figure 1: CWG algorithm to identify sites amenable to glycosylation.** (A) SARS-CoV-2 spike trimer (grey)
545 decorated with native glycans (blue) with one RBD in the up state (green) binding to ACE2 (orange) and
546 detailed cartoon representation of RBD with native glycan bound to ACE2. Schematic of wild type glycan
547 distribution across the entire spike. (B) CWG pipeline for assessing PNGS on the RBD. (C) Rosetta scores
548 of glycosylated RBDs for normalized solvent accessible surface (SASA) and residue clash score (fa_rep of
549 sugar residues). (D) Protein folding (total Rosetta score) vs Glycan score (fa_rep of sugar and protein) for
550 each of the glycosylated RBDs selected in (C). Selection criteria shown as dashed lines in (C) and (D).

551 **Figure 2: In vitro characterization of single glycan variants of RBD.** (A) Model of selected glycan sites
552 (blue spheres) on the RBD (green cartoon) interacting with ACE2 binding helices (orange cartoon). (B)
553 Small scale screen of selected variants binding to ACE2 in Area Under the Curve from ELISA binding curves
554 and normalized to WT binding (bars), qualitative expression from Western Blot represented as +/- symbols
555 above the bars. (C) Neutralizing epitopes mapped on RBD structure with RBD in grey surface and ACE2
556 binding helices in orange, surface patches are color according to: RBD-A,B,C are in orange; RBD-D in red;
557 RBD-E in green, RBD-F in blue. (D) SPR binding kinetics of single glycan variants to a panel of SARS-CoV-2
558 antibodies. (E) Relative binding as measured by ELISA EC50 ratio of glycan variants binding to WT RBD
559 binding in a panel of neutralizing and non-neutralizing antibodies. Blue to Red coloring was done based
560 on stronger or weaker binding relative to WT RBD.

561 **Figure 3: In vitro and in vivo antigenic profile of multiglycan RBDs.** (A) Surface representation of RBD
562 (green) bound to ACE2 (blue cartoons) with glycans (green for native and blue for designed in lines) for
563 the WT RBD and RBD g5.1 constructs. (B) Relative binding as measured by ELISA EC50 ratio of glycan
564 variants binding to a panel of neutralizing and non-neutralizing antibodies to WT RBD binding. Blue to Red

565 coloring was done based on stronger or weaker binding relative to WT RBD. (C) Antibody binding titers
566 and (D) pseudovirus ID₅₀ neutralization titers from BALB/c mice immunized with 25µg of plasmids
567 encoding WT RBD or RBD g5.1 at week 0 and 2. (E) ACE2 competition assay layout for measuring blocking
568 of ACE2 interacting with RBD with RBS-directed antibodies from the sera of vaccinated mice. (F) Fraction
569 of ACE2 binding blocked by antibodies in ACE2 competition assay and (G) Blocking titer measured as the
570 first dilution of sera at which a reduction in ACE2 binding is observed. (unpaired two tailed Student t-test
571 (F) p = 0.0020, (G) p = 0.0236).

572 **Figure 4: Immune focused RBD nanoparticle structure and immunogenicity.** (A) Models of 8 different
573 RBD nanovaccines. In each model, the coloring is as follows: RBS (yellow) on the RBD (green) coated with
574 glycans (blue) fused with a glycine-serine linker (gray) to a nanoparticle scaffold (red). (B) Endpoint titers
575 for a single BALB/c mouse immunized with once with 2 µg of plasmid encoding RBD nanoparticles by DNA-
576 E.P. colored as indicated on the figure, in vitro expression and assembly of nanoparticles indicated in the
577 'ASM' column as either expressed/assembled (A), poor expression/assembly (X) or not tested (N). (C) Size-
578 exclusion chromatogram and multiangle light scattering of RBD g5.1 multimers (Black line under each
579 curve indicates molecular weight and correspond to the right y-axis). (D) 2D class averages showing RBDs
580 decorating the RBD g5.1 24mer. (E) Cryo-EM density map of RBD g5.1 24mer at low threshold, the 24mer
581 scaffold could be unambiguously determined (Figure S9), the flexible linker attachment points for the
582 RBDs on the 24mer scaffold could be observed at low density threshold (blue dots) (F) Endpoint titers
583 for expanded groups (n=5) of BALB/c mice immunized with 2µg of plasmid encoding RBD nanoparticles
584 by DNA-E.P. (G) Pseudovirus neutralization of SARS-CoV-2 variants B.1(WT), B.1.351, B.1.7.1 and P.1 by
585 sera from BALB/c mice immunized with 5µg RBD g5.1 24mer. (H) Endpoint binding titers developed in
586 BALB/c mice immunized with 2µg of P.1 RBD g5.1 nanoparticle (I) Pseudovirus neutralization of SARS-CoV-
587 2 variants by sera from BALB/c mice immunized with P.1 RBD g5.1

588 **Figure 5: Lethal challenge of SARS-CoV-2 in rodent model.** (A) K18 hACE2 lethal challenge study overview
589 (B) SARS-CoV-2 live virus neutralization one day prior to challenge. **** p < 0.0001. (C) Weight loss of K18
590 hACE2 mice after SARS-CoV-2 challenge. (D) Kaplan-Meier curves representing survival of K18 hACE2 mice
591 after SARS-CoV-2 challenge. (Mantel-Cox test vs. naïve: RBD monomer p = 0.0327, RBD g5.1 24mer p =
592 0.0006, RBD g5.1 120mer 1 µg p = 0.0087, RBD g5.1 120mer 5 µg p = 0.0006; vs. RBD monomer: RBD g5.1
593 120mer 5 µg p = 0.0426, RBD g5.1 24mer p = 0.0048) (E) Pseudovirus neutralization titers of surviving and
594 non-surviving mice. (unpaired two-tailed Student t-test p = 0.0003) (F) Correlation between body weight
595 change at day 4 post-challenge and pre-challenge live virus neutralizing titers (ID₅₀). (G) Viral titers in nasal

596 turbinates, brain and lung tissue at day 4 post challenge. (unpaired two-tailed Student t-test vs. naïve:
597 RBD 120mer 1 μg $p = 0.0110$, RBD 120mer 5 μg $p = 0.0109$, RBD g5.1 24mer $p = 0.0110$). LOD for this assay
598 (lower dashed line) is lower than the LOD reported elsewhere (top dashed line).

599 **Figure 6: Humoral responses to nanovaccines in OmniMouse[®], Guinea Pigs and Hamsters.** (A) Human
600 antibody titers from OmniMouse[®] immunized three times four weeks apart with 25 μg of DNA encoding
601 RBD nanoparticles as measured by combined AUC from ELISA curves with human IgK and human IgL
602 secondaries. (B) as measured by endpoint titer using human IgK and human IgL secondaries (C) Pseudo
603 virus neutralization titers at week 6 and week 8 post immunization (D) Endpoint titers against RBD for sera
604 from Hartley guinea pigs immunized with RBD monomer and RBD g5.1 24mer after a single dose (E)
605 Pseudo virus neutralization of sera from guinea pigs immunized with RBD monomer and RBD g5.1 24mer
606 after a single dose (unpaired t-test vs. naïve: 5 μg RBD g5. 1 24mer week 2 $p=0.0140$, week 3 $p=0.0003$,
607 week 4 $p=0.0146$; 10 μg RBD g5. 1 24mer: wk 2 $p=0.0145$, week 3 $p=0.0016$, week 4 $p=0.0007$. Unpaired
608 t-test vs 10 μg RBD to 5 μg RBD g5. 1 24mer week 2 $p=0.0142$, week 3 $p=0.0104$; 10 μg RBD g5. 1 24mer
609 week 2 $p=0.0002$, week 3 $p=0.0042$, week 4 $p=0.0304$. (F) Endpoint binding titers against RBD for sera
610 from Syrain Golden hamsters immunized with RBD monomer or RBD 48mer two times with two different
611 doses (G) Neutralization of SARS-CoV-2 pseudovirus by sera from hamsters immunized with RBD
612 monomer or RBD 48mer with two different doses. (unpaired two-tailed Student t-test: RBD 48mer 10 μg
613 vs. RBD monomer 10 μg $p = 0.0079$, RBD 48mer 2 μg vs. RBD monomer 2 μg $p = 0.0004$) (H) Lung lavages
614 from hamsters immunized with RBD monomer or RBD 48mer.

615 **Supplementary Figure 1: Modeling and Survey of native glycans on human virus proteins.** (A) Native
616 glycans were modeled on PNGS using our modified Rosetta GlycanTreeModeler script on four human viral
617 glycoproteins: envelope of HIV, hemagglutinin of H1N1, and Spike proteins of SARS-CoV and MERS-CoV.
618 (B) Repulsive glycan energy of individual modeled glycans on each native PNGS sites were surveyed and a
619 cut-off value of 5.0 (REU) is used to include all possible native glycosylation scenarios.

620 **Supplementary Figure 2: Rationale for generating glycan combinations.** (A) Distance map of all residue
621 pairs on native RBD to approximate distances between two engineered glycans. Distance between the
622 geometric center of each residue of any residue pair on RBD is calculated using PyRosetta script. The
623 distance information is subsequently visualized as a Distance Heatmap in R. Only glycans that are 10-20
624 Angstroms away from each other can be selected for a combination. (B) An example of distance
625 measurements for a combination of three glycan additions where the residue of added glycans (red

626 spheres) is on RBD (green) bound to two helices of ACE2 (orange) with one native glycan (blue). Distances
627 between each engineered glycan is shown in black dash and labeled with the distance value in Angstroms.
628 (C) A table summary of all combinations made in this study with glycan addition positions and distance
629 between engineered glycans.

630 **Supplementary Figure 3: WT RBD nanoparticles and pseudovirus neutralization of expanded groups**
631 **(n=5) in BALB/c mice.** (A) Size exclusion chromatograms for WT RBD nanoparticles. (B) Endpoint titers
632 from binding ELISA to RBD of immunizations with 2 μ g of DNA-launched WT RBD nanoparticles. (C)
633 Pseudovirus neutralization of BALB/c mice immunized (n=5 or 10) with 2 μ g immune focused DNA-
634 launched nanoparticles. * p < 0.05 (Two-way ANOVAs vs. RBD: RBD g8.2 7mer p = 0.0111, RBD g5.1 24mer
635 p = 0.0205, RBD g8.2 24mer p = 0.0199, RBD g8.2 60mer p = 0.0135).

636 **Supplementary Figure 4: Immunogenicity of RBD nanovaccines in C57BL/6 mice.** Endpoint titers (A) and
637 pseudo virus neutralization ID50s (B) for C57BL/6 mice immunized with 1 μ g or 5 μ g of four selected RBD
638 nanovaccines. (C) IFN- γ ELISpot assay with splenocytes from mice immunized with RBD monomer, RBD
639 g5.1 24mer, and RBD g5.1 120mer vaccines, or the naïve. Intracellular staining of IFN- γ (D), surface staining
640 of CD107a (E), and intracellular staining of TNF α (F) of effector memory CD8+ CD44+ CD62- T cells from
641 splenocytes. Error bars indicate means \pm SD (n = 3 - 5 mice/group). Splenocytes were stimulated by native
642 RBD peptides in B, C, and D. ((C) unpaired two-tailed Student t-tests vs. naïve: RBD monomer p = 0.0063,
643 RBD g5.1 24mer p = 0.0049, RBD g5.1 120mer 1 μ g p < 0.0019, RBD g5.1 120mer 5 μ g p < 0.0001). ((D)
644 unpaired two-tailed Student t-tests vs. naïve: RBD monomer p < 0.0001, RBD g5.1 24mer p = 0.0010, RBD
645 g5.1 120mer 1 μ g p = 0.0005, RBD g5.1 120mer 5 μ g p < 0.0001; vs. RBD Monomer: RBD g5.1 120mer 5 μ g
646 p = 0.0123). ((E) unpaired two-tailed Student t-tests vs. naïve: RBD monomer p = 0.0007, RBD g5.1 24mer
647 p = 0.0018, RBD g5.1 120mer 1 μ g p = 0.0031, RBD g5.1 120mer 5 μ g p < 0.0001; vs. RBD Monomer: RBD
648 g5.1 120mer 5 μ g p = 0.0063). ((F) unpaired two-tailed Student t-tests vs. naïve: RBD monomer p = 0.0013,
649 RBD g5.1 24mer p = 0.0153, RBD g5.1 120mer 1 μ g p = 0.0038, RBD g5.1 120mer 5 μ g p = 0.0002).

650 **Supplementary Figure 5: Protein nanoparticle immunization.** Endpoint titers of BALB/c mice immunized
651 SC with 10 μ g of RBD g8.2 7mer and 24mer protein co-formulated with RIBI adjuvant.

652 **Supplementary Figure 6: Emerging variants of concern.** (A) Endpoint titers of BALB/c mice immunized
653 with 5 μ g of RBD g5.1 24mer (WT RBD) binding to WT, B.1.351, B.1.1.7., and P.1 RBDs and individual
654 mutation RBDs. (B) SEC trace of P.1 RBD g5.1 24mer. (C) Comparison of neutralization of BALB/c mice
655 immunized with RBD monomer 2 μ g and Spike 10 μ g against variant pseudoviruses.

656 **Supplementary Figure 7: Pre-challenge pseudo virus neutralization of K18 hACE2 mice.** Pseudo virus
657 neutralization of week 3 sera from K18 hACE2 mice immunized for challenge study.

658 **Supplementary Figure 8: Additional Omni mice serology.** (A) AUC of binding ELISAs from Omni mice
659 immunized with DNA-launched RBD nanoparticles with mIgG, rIgM, and rIgG breakdown. (B) AUC of
660 binding ELISAs from Omni mice with hIgL and hIgK breakdown. (C) Murine leukemia virus (MLV)
661 neutralization of Omni mice immunized with DNA-launched RBD nanoparticles demonstrate no
662 nonspecific neutralization.

663 **Supplementary Figure 9: Cryo-EM of RBD g5.1 24mer immunogen.** Cryo-EM data processing followed
664 standard routines. 3D reconstruction was performed under assumption of octahedral symmetry as well
665 as asymmetrically. The two resulting density maps demonstrate flexible linker attachment points at low
666 density threshold at identical places. Final resolutions were 3.4Å and 3.9Å, respectively as can be
667 confirmed by visual inspection of the density close-ups. Density for RBDs is disordered due to the inherent
668 flexible linker in our immunogen design.

669

670 **Table 1. Kinetic constants for RBD-antibody interactions modeled well by 1:1 Langmuir fitting.**

671

672 **Funding Sources**

673 This research including design of nanoparticles was supported by Wistar Coronavirus Discovery Fund and
674 CURE/PA Dept Health grant (SAP# 4100083104) awarded to D.W.K. The DNA immunizations were
675 supported by NIH/NIAID CIVICs (75N93019C00051), Wistar Coronavirus Discovery Fund, Wistar SRA 16-4
676 / Inovio Pharmaceuticals awarded to D.B.W. This research was supported by Indiana University start-up
677 funds to J.P. The funding sources were not involved in the design of this study, collection and analyses of
678 data, or decision to submit the manuscript.

679

680 **Conflicts of Interest**

681 T. Smith, K. Schultheis K.E. Broderick and L. Humeau are employees of Inovio Pharmaceuticals and as
682 such receive salary and benefits, including ownership of stock and stock options, from the
683 company. C. Iffland is an employee of Ligand Pharmaceuticals Inc. and as such receives salary and
684 benefits from the company., D.W. Kulp reports a patent for nanoparticle vaccine pending. D.B.W. has
685 received grant funding, participates in industry collaborations, has received speaking honoraria,
686 and has received fees for consulting, including serving on scientific review committees and board
687 services. Remuneration received by D.B.W. includes direct payments or stock or stock options,
688 and in the interest of disclosure he notes potential conflicts associated with this work with Inovio
689 and possibly others. In addition, he has a patent DNA vaccine delivery pending to Inovio. No
690 potential conflicts of interest were disclosed by the other authors.

691

692 **Acknowledgments**

693 The authors would like to thank the The Wistar Institute Core facilities for providing care to the animals.
694 We would like to acknowledge Dr. Jason S. McLellan for providing reagents for hamster serology. We
695 would also like to thank Dr. Jared Adolf-Bryfogle for generously contributing GTM code to Rosetta for use
696 in this project.

697 **Author Contributions**

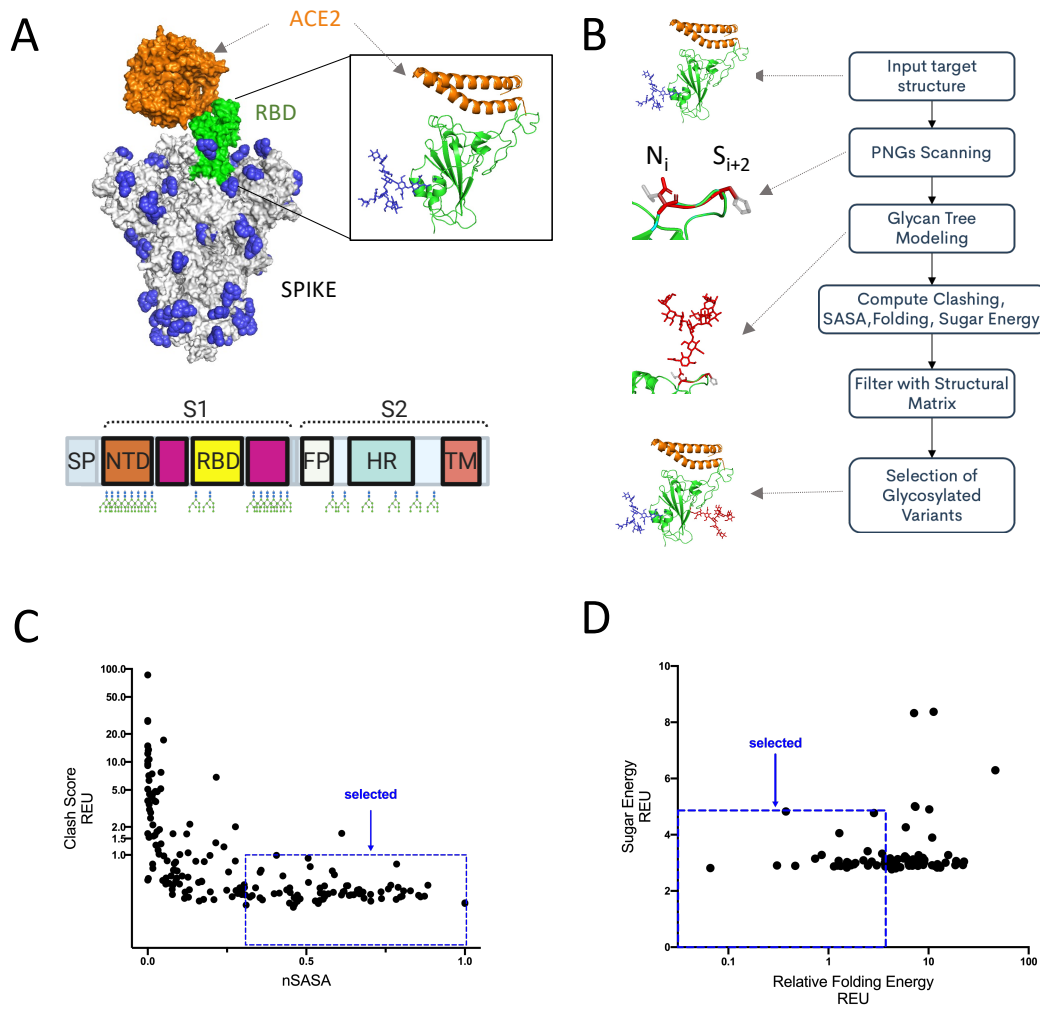
698 K.M.K., Y.W. and D.W.K. designed immunogens. K.M.K, K.L., Z.X., S.N.W., X.Z., N.C., N.T., M.P., J.P., E.L.R.,
699 D.F., C.I. D.B.W and D.W.K. planned experiments. K.M.K., K.L., Z.X., S.N.W., X.Z., N.C., N.T., M.P., J.P., J.D.,
700 A.M., E.L.R. and D.F conducted experiments. K.S., K.E.B., L.H., and T.S. contributed resources for lethal
701 challenge study. C.I. contributed resources for the human antibody transgenic mouse study. K.M.K., K.L.,
702 Z.X., S.W., X.Z., N.C., N.T., M.P., J.P., E.L.R., J.D., A.M., D.F. and D.W.K. analyzed the data. K.M.K. and D.W.K.
703 wrote the article. K.M.K, K.L., Y.W., S.N.W., N.C., J.D., A.M., J.P., D.B.W. , and D.W.K. edited the article.

704

705

706

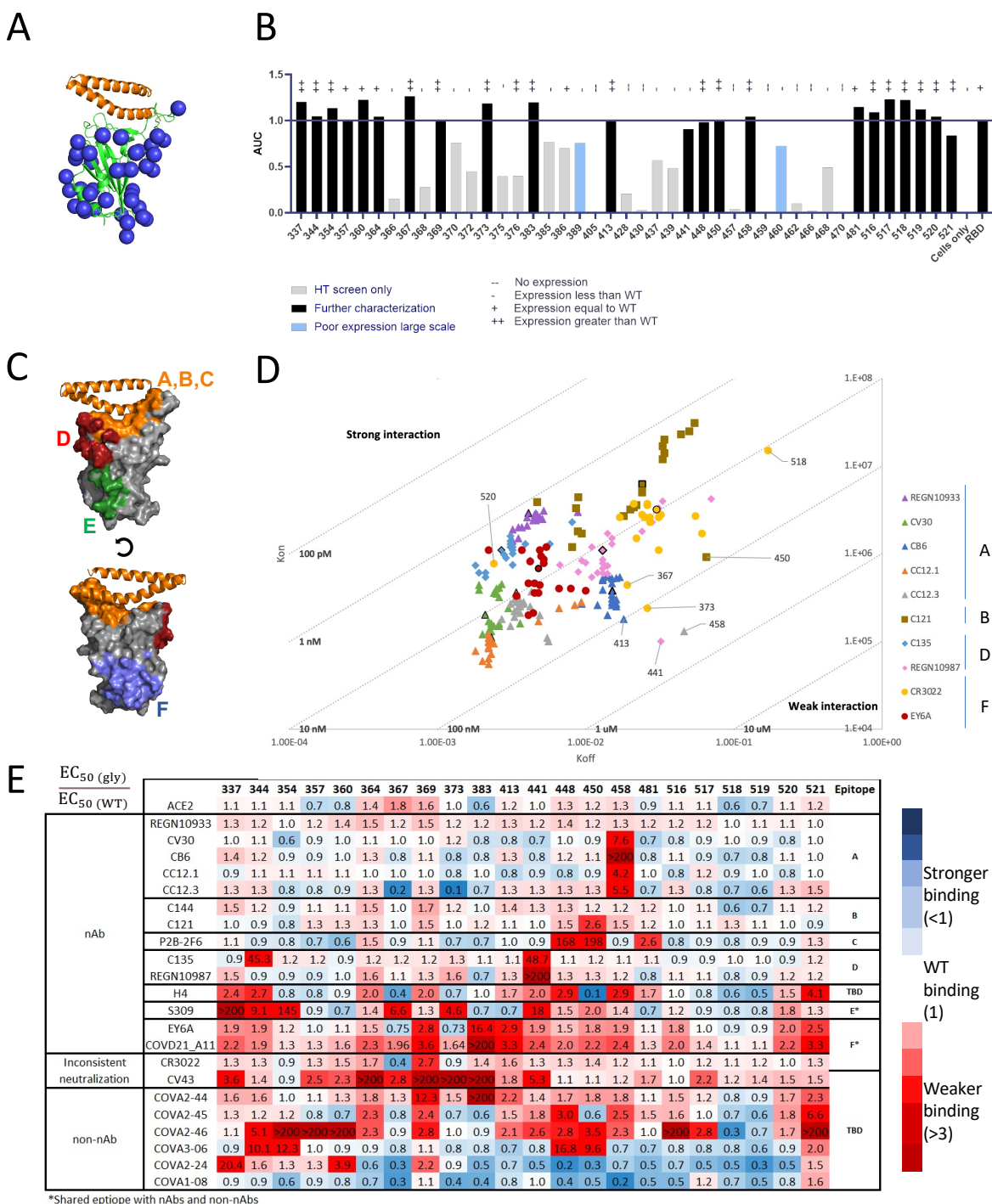
707 **Figure 1**



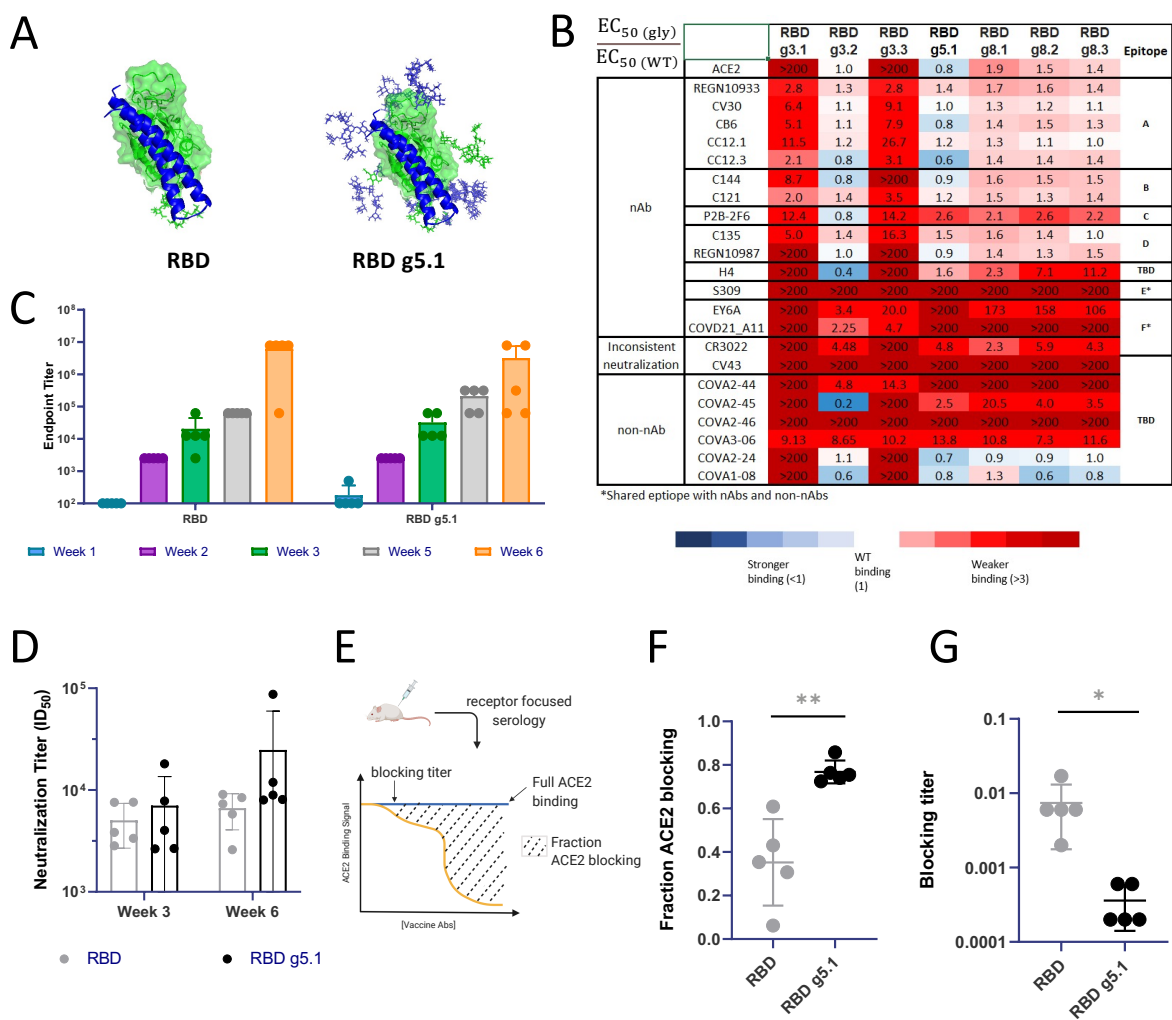
708

709

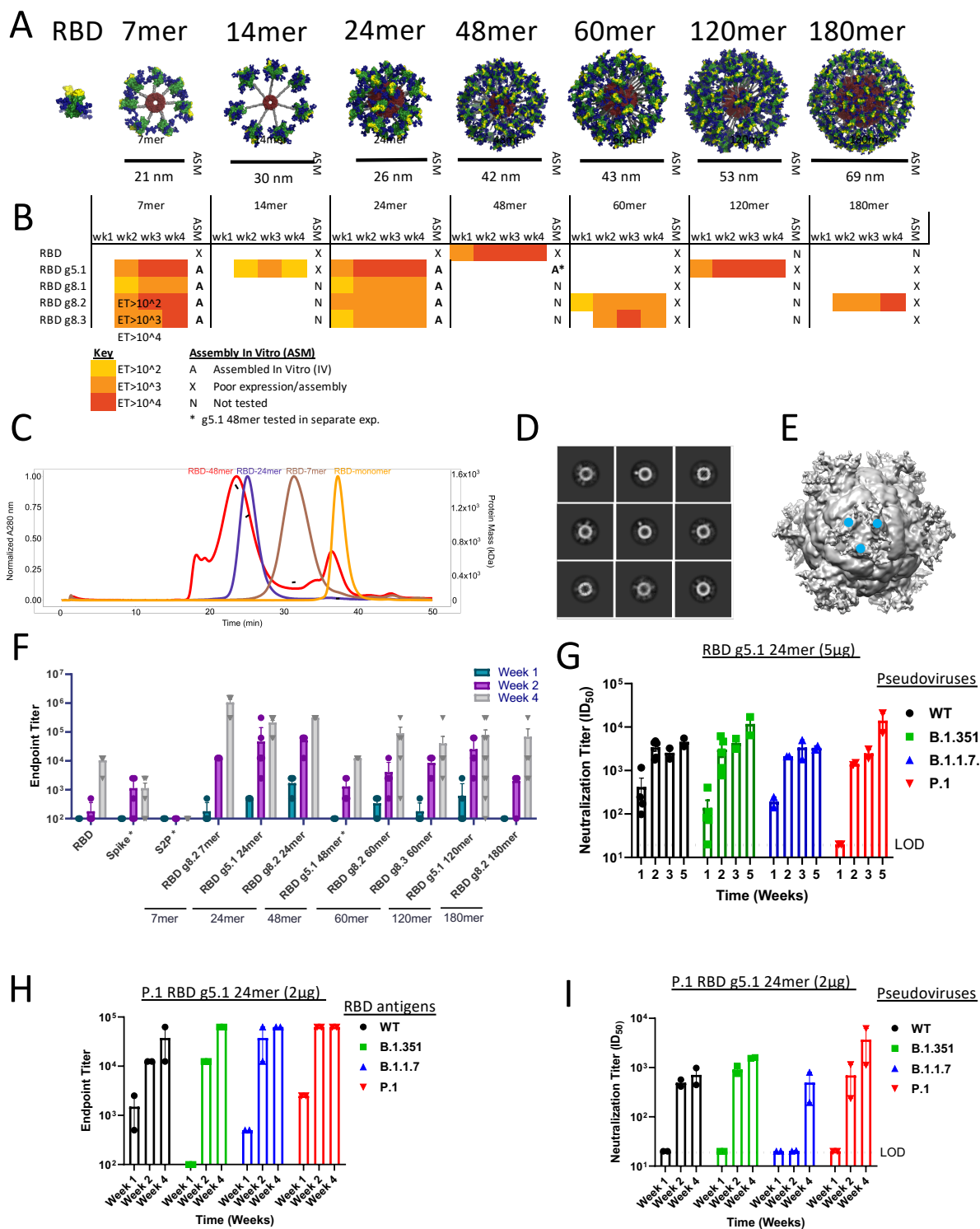
710 Figure 2



713 **Figure 3**



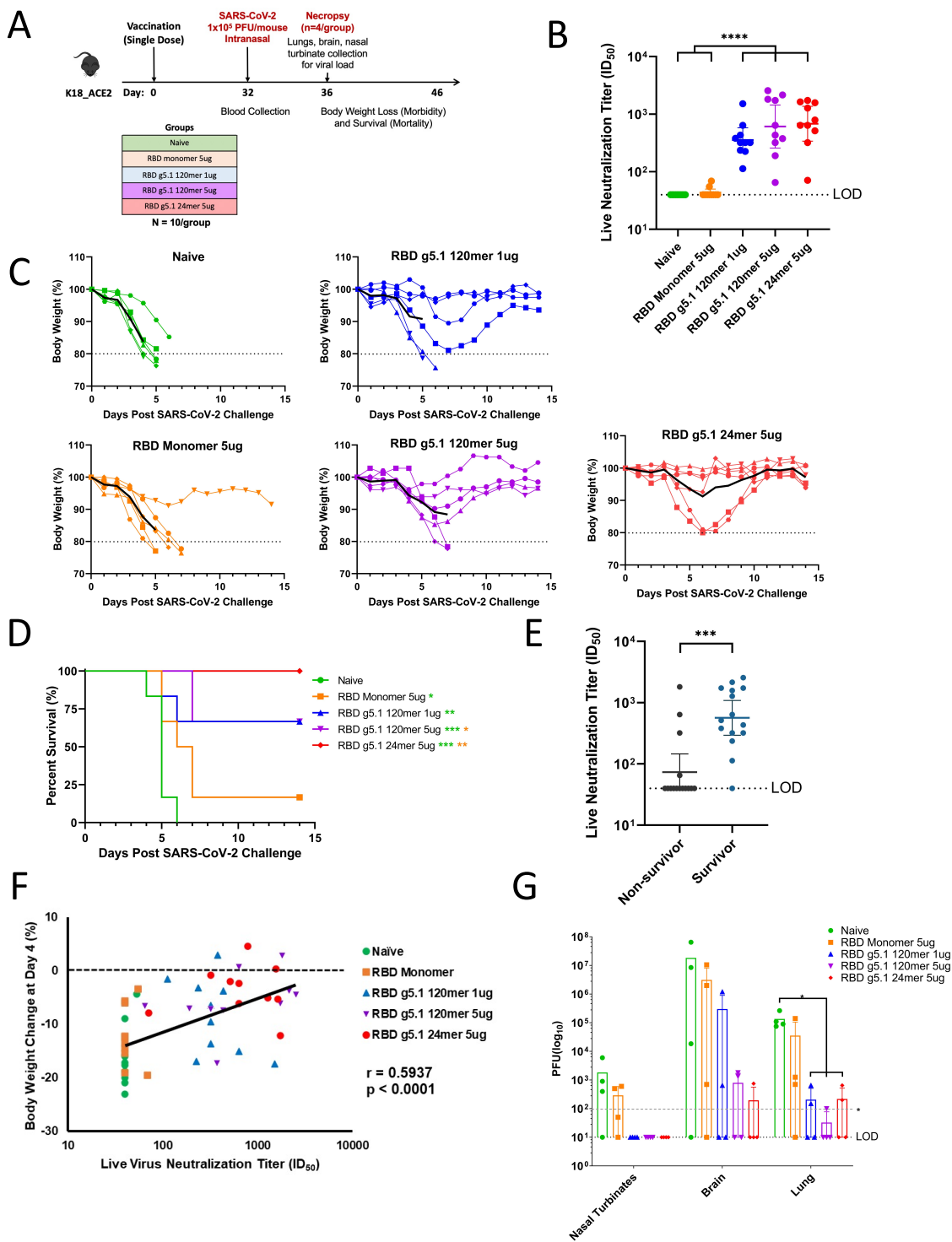
716 **Figure 4**



717

718

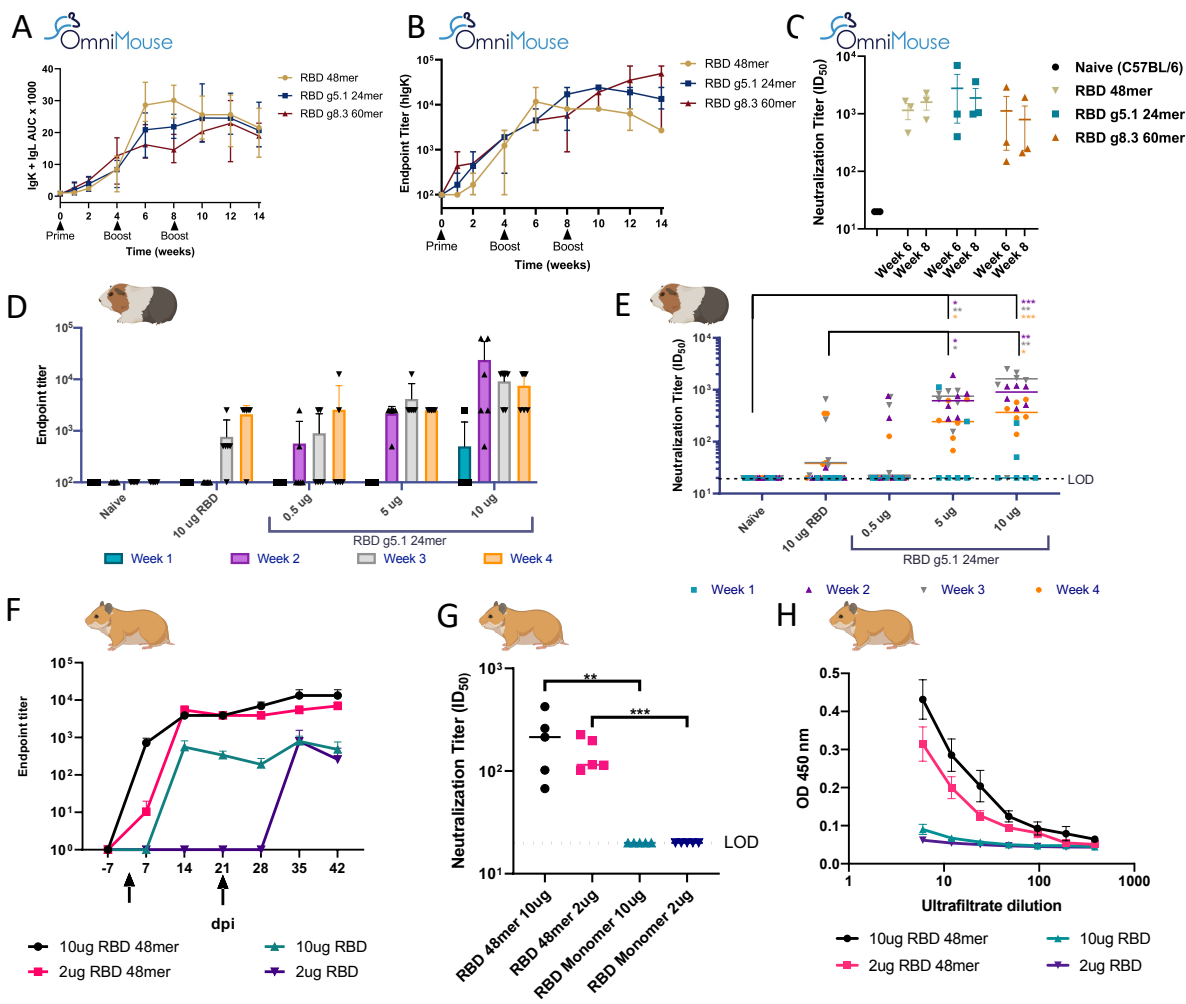
719 **Figure 5**



720

721

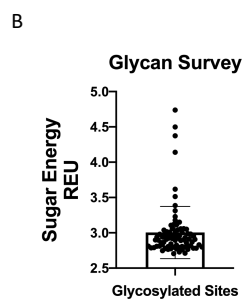
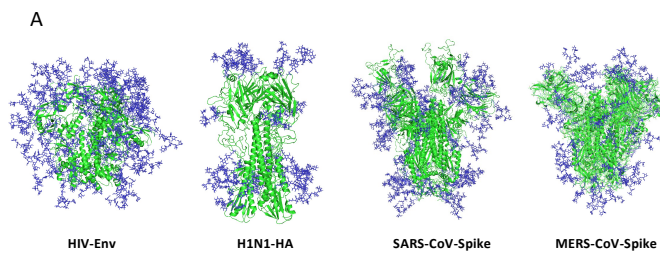
722 **Figure 6**



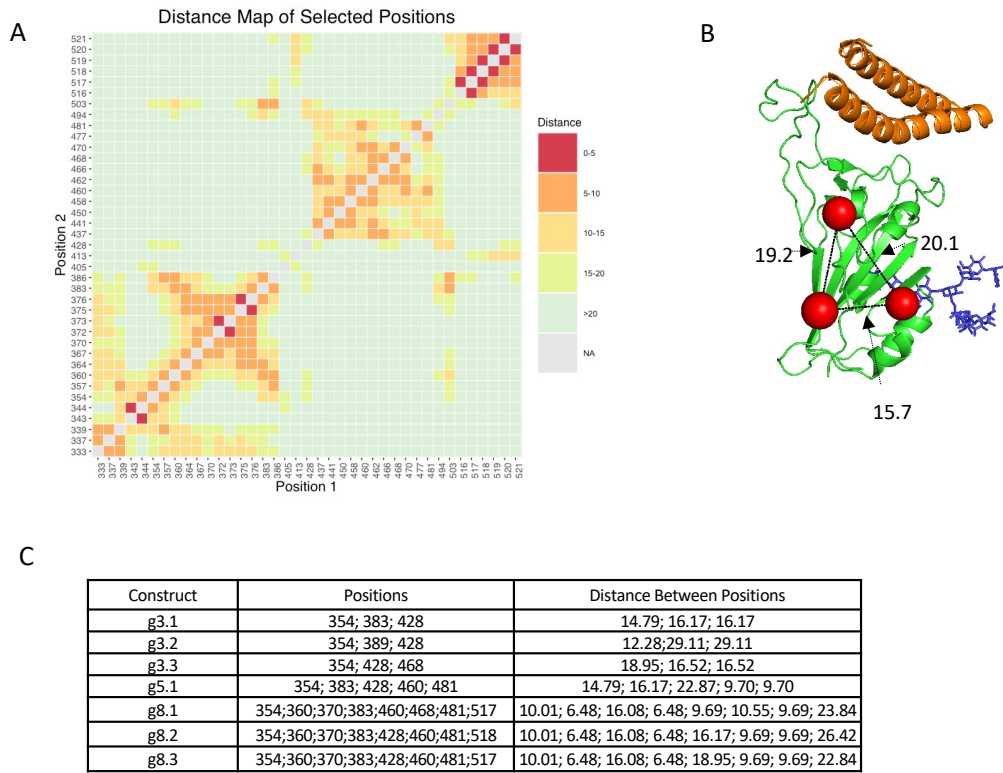
723

724

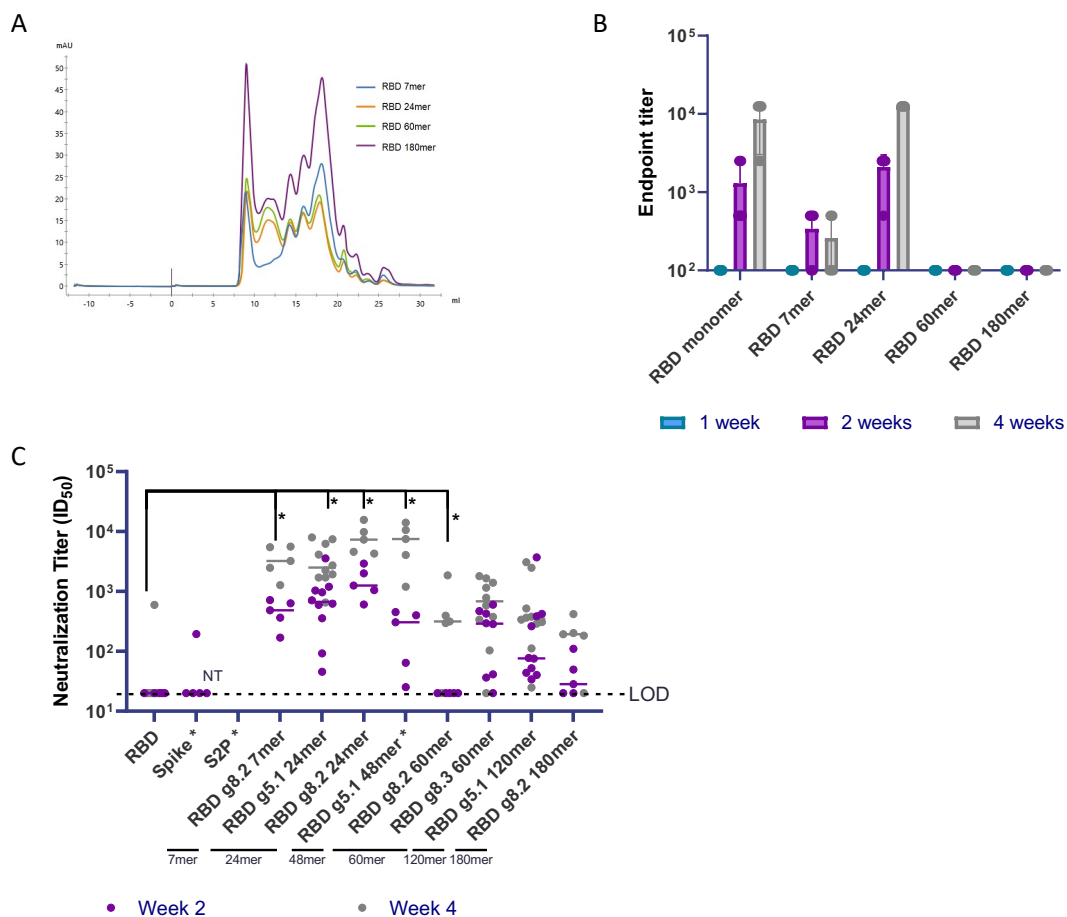
725 **Figure S1**



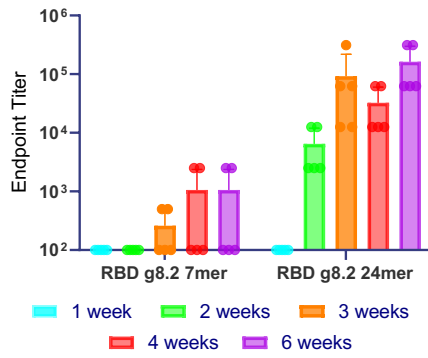
728 **Figure S2**



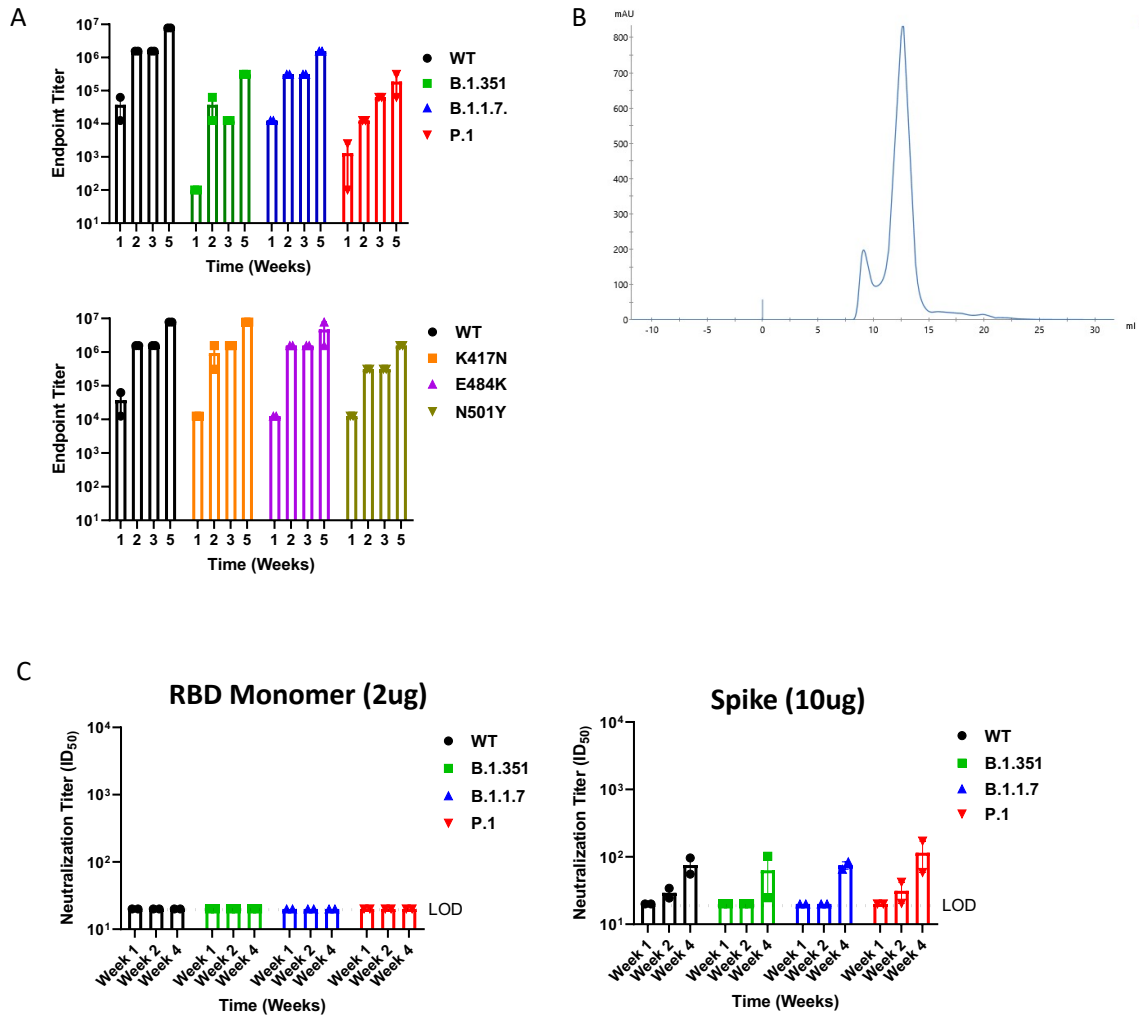
731 **Figure S3**



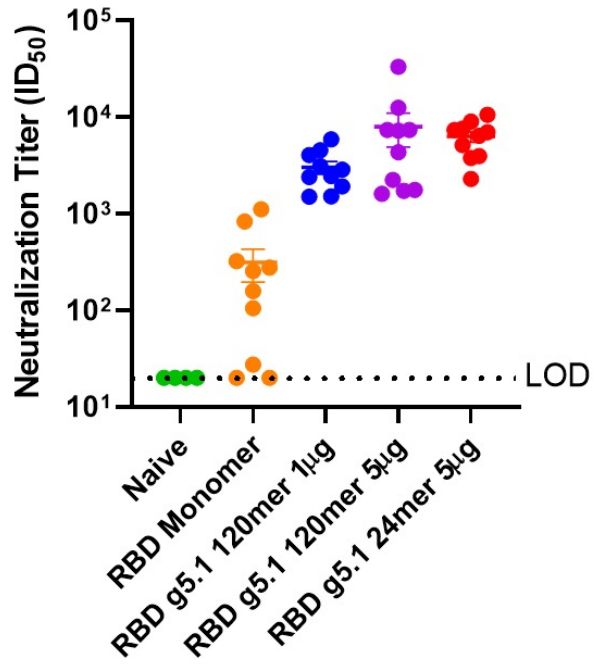
737 **Figure S5**



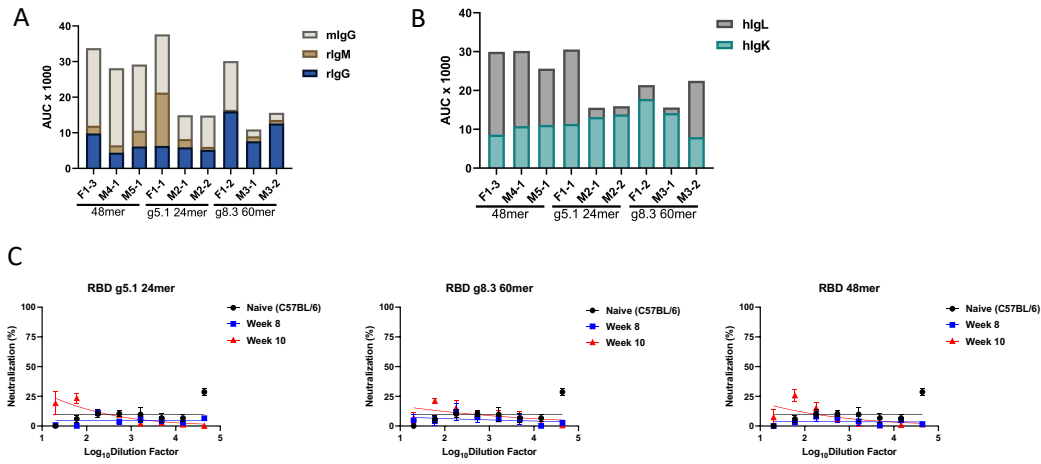
740 Figure S6



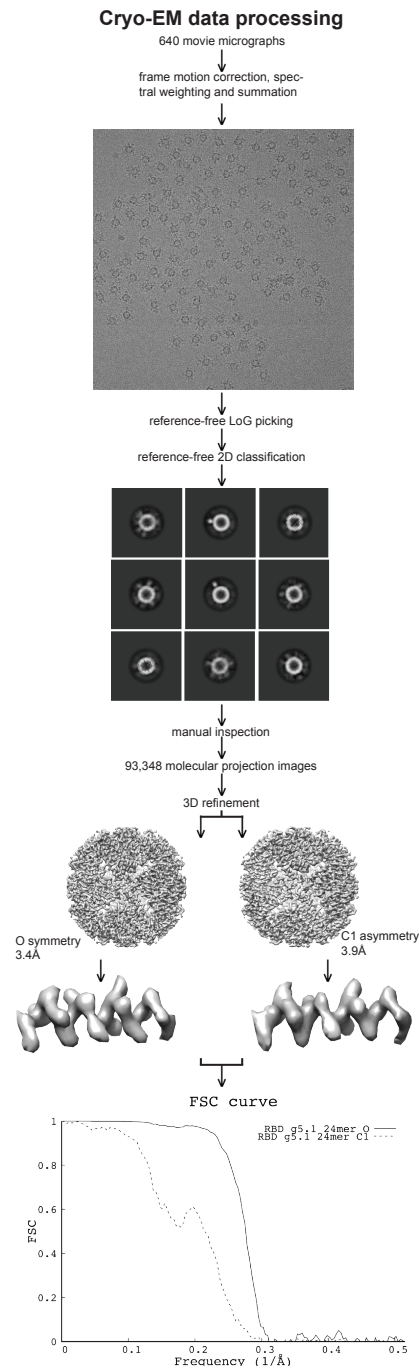
743 Figure S7



746 **Figure S8**



749 **Figure S9**



750
751

752 Table S1

Epitope	Antibody	Construct	Koff	Kon	Corrected KD (nM)				
A	REGN10933	RBD	4.10E-03	2.90E+06	1.4				
		337	4.50E-03	2.50E+06	1.8				
		344	4.70E-03	2.70E+06	1.7				
		354	4.70E-03	2.60E+06	1.8				
		357	5.10E-03	2.50E+06	2.1				
		360	4.60E-03	2.90E+06	1.6				
		364	4.40E-03	2.40E+06	1.8				
		367	3.50E-03	2.00E+06	1.7				
		369	5.10E-03	2.50E+06	2				
		373	4.00E-03	2.10E+06	1.9				
		383	4.50E-03	2.60E+06	1.7				
		413	4.80E-03	2.60E+06	1.8				
		441	4.60E-03	2.40E+06	1.9				
		448	4.90E-03	2.60E+06	1.8				
		450	8.80E-03	3.00E+06	3				
		458	3.70E-03	2.00E+06	1.9				
		481	3.20E-03	1.90E+06	1.7				
		516	4.70E-03	2.80E+06	1.7				
		517	3.50E-03	1.50E+06	2.3				
		518	5.20E-03	3.10E+06	1.7				
		519	4.50E-03	2.80E+06	1.6				
		520	4.00E-03	2.60E+06	1.5				
		521	3.20E-03	1.40E+06	2.4				
		A	CV30	RBD	2.10E-03	2.00E+05	10		
				337	2.50E-03	3.50E+05	7.2		
				344	2.20E-03	1.30E+05	16		
				354	2.30E-03	1.50E+05	16		
				357	2.60E-03	3.20E+05	8		
				360	2.30E-03	1.60E+05	14		
				364	2.40E-03	3.60E+05	6.8		
				367	2.40E-03	1.50E+05	16		
				369	2.30E-03	1.30E+05	17		
				373	2.00E-03	1.20E+05	17		
				383	2.50E-03	4.00E+05	6.2		
				413	3.00E-03	2.40E+05	12		
				441	2.30E-03	1.60E+05	15		
				448	2.60E-03	4.10E+05	6.3		
				450	3.60E-03	1.60E+05	23		
				458	ND	ND	ND		
				481	2.60E-03	1.60E+05	16		
				516	1.90E-03	3.90E+05	5		
				517	2.60E-03	1.50E+05	17		
				518	2.70E-03	4.50E+05	6		
				519	2.20E-03	1.70E+05	13		
				520	1.90E-03	4.40E+05	4.3		
				521	2.20E-03	1.20E+05	19		
				A	CB6	RBD	1.50E-02	3.80E+05	39
						337	1.30E-02	5.20E+05	25
						344	1.60E-02	2.70E+05	60
						354	1.60E-02	2.50E+05	65
						357	1.60E-02	5.30E+05	30
						360	1.50E-02	2.80E+05	54
364	1.40E-02					5.50E+05	26		
367	1.40E-02					2.00E+05	68		
369	1.50E-02					4.60E+05	31		
373	1.50E-02					2.60E+05	57		
383	1.50E-02					3.10E+05	48		
413	1.80E-02					1.80E+05	97		
441	1.30E-02					5.00E+05	27		
448	1.20E-02					2.60E+05	47		
450	1.30E-02					5.00E+05	25		
458	ND					ND	ND		
481	1.50E-02					5.20E+05	29		
516	1.50E-02					3.40E+05	46		
517	1.70E-02					5.40E+05	31		
518	1.60E-02					3.00E+05	53		
519	1.40E-02					5.80E+05	24		
520	9.40E-03					2.70E+05	35		
521	1.30E-02					3.90E+05	34		
A	CC12.1					RBD	2.30E-03	1.10E+05	20
						337	2.20E-03	1.00E+05	21
						344	8.40E-03	2.60E+05	32
						354	9.30E-03	2.80E+05	33
						357	2.30E-03	9.80E+04	23
						360	6.60E-03	2.40E+05	28
		364	2.20E-03			1.20E+05	19		
		367	NT			NT	NT		
		369	2.20E-03			6.40E+04	35		
		373	NT			NT	NT		
		383	2.20E-03			8.60E+04	25		
		413	2.20E-03			5.50E+04	40		
		441	2.20E-03			8.60E+04	26		
		448	4.80E-03			1.70E+05	28		
		450	2.40E-03			9.50E+04	25		
		458	ND			ND	ND		
		481	2.20E-03			1.10E+05	21		
		516	2.20E-03			9.80E+04	22		
		517	2.30E-03			7.20E+04	31		
		518	2.20E-03			8.30E+04	27		
		519	2.20E-03			1.20E+05	18		
		520	1.80E-03			7.80E+04	23		
		521	2.00E-03			6.00E+04	34		
		B	CC12.3			RBD	3.40E-03	3.60E+05	9.6
						337	3.60E-03	2.90E+05	12
						344	3.40E-03	2.20E+05	15
						354	3.60E-03	2.10E+05	17
						357	4.20E-03	2.50E+05	16
						360	3.50E-03	2.50E+05	14
				364	3.80E-03	2.80E+05	14		
				367*	5.50E-03	1.10E+05	50		
				369	2.70E-03	1.80E+05	15		
				373*	5.60E-03	1.00E+05	54		
				383	3.40E-03	2.80E+05	12		
				413	4.90E-03	2.00E+05	25		
				441	3.30E-03	1.90E+05	17		
				448	3.60E-03	2.50E+05	14		
				450	3.60E-03	2.70E+05	13		
				458	4.60E-02	1.30E+05	360		
				481	3.30E-03	2.20E+05	15		
				516	3.30E-03	3.00E+05	11		
				517	4.30E-03	3.70E+05	12		
				518	3.60E-03	2.60E+05	14		
				519	3.80E-03	2.70E+05	14		
				520	3.10E-03	2.70E+05	11		
				521	3.10E-03	1.50E+05	20		
				B	C121	RBD	2.40E-02	6.20E+06	3.9
						337	5.40E-02	3.10E+07	1.7
						344	8.80E-03	1.80E+06	4.9
						354	9.40E-03	1.70E+06	5.6
						357	3.40E-02	1.40E+07	2.4
						360	2.40E-02	5.00E+06	4.7
364	8.90E-03					4.40E+06	2		
367	NT					NT	NT		
369	1.80E-02					2.70E+06	6.5		
373	NT					NT	NT		
383	3.30E-02					1.70E+07	2		
413	5.00E-02					2.50E+07	2		
441	2.10E-02					3.40E+06	6.3		
448	8.60E-03					3.30E+06	2.6		
450	6.50E-02					9.20E+05	70		
458	3.30E-02					1.20E+07	2.7		
481	2.00E-02					3.20E+06	6.5		
516	3.40E-02					2.00E+07	1.7		
517	2.20E-02					3.60E+06	6.3		
518	4.40E-02					2.30E+07	1.9		
519	2.40E-02					5.20E+06	4.7		
520	4.70E-03					3.90E+06	1.2		
521	8.10E-03					1.20E+06	6.5		
B	C135					RBD	2.70E-03	1.10E+06	2.4
						337	3.10E-03	1.40E+06	2.2
						344	ND	ND	ND
						354	ND	ND	ND
						357	3.10E-03	1.20E+06	2.7
						360	2.10E-03	6.10E+05	3.4
		364	3.90E-03			1.30E+06	2.9		
		367	8.10E-03			2.30E+06	3.5		
		369	2.90E-03			9.00E+05	3.2		
		373	2.10E-03			5.40E+05	3.9		
		383	3.10E-03			1.30E+06	2.3		
		413	1.90E-03			6.10E+05	3.2		
		441	ND			ND	ND		
		448	3.20E-03			7.50E+05	4.2		
		450	5.70E-03			1.30E+06	4.4		
		458	3.20E-03			1.10E+06	2.9		
		481	3.20E-03			1.20E+06	2.6		
		516	3.10E-03			1.60E+06	1.9		
		517	4.20E-03			8.40E+05	5		
		518	ND			ND	ND		
		519	2.80E-03			9.80E+05	2.9		
		520	1.80E-03			7.40E+05	2.4		
		521	3.20E-03			1.00E+06	3.1		
		D	REGN10987			RBD	1.30E-02	1.10E+06	12
						337	1.10E-02	1.20E+06	9.1
						344	1.20E-02	6.10E+05	20
						354	1.30E-02	6.80E+05	19
						357	2.40E-02	1.80E+06	13
						360	1.30E-02	7.80E+05	17
				364	1.50E-02	1.30E+06	11		
				367	1.00E-02	7.90E+05	13		
				369	1.40E-02	5.90E+05	23		
				373	9.40E-03	8.40E+05	11		
				383	3.30E-02	4.00E+06	8.4		
				413	3.10E-02	3.30E+06	9.4		
				441	3.20E-02	1.00E+05	310		
				448	7.00E-02	4.20E+06	17		
				450	8.90E-03	6.20E+05	14		
				458	2.80E-02	2.30E+06	12		
				481	1.40E-02	7.30E+05	20		
				516	1.40E-02	1.70E+06	8.3		
				517	1.30E-02	6.00E+05	22		
				518	1.50E-02	1.50E+06	10		
				519	1.30E-02	8.60E+05	15		
				520	6.70E-03	7.50E+05	8.9		
				521	1.10E-02	5.40E+05	21		
				F	CR3022	RBD	3.00E-02	3.20E+06	9.6
						337	1.70E-02	2.60E+06	6.7
						344	3.10E-02	2.60E+06	12
						354	2.70E-02	2.30E+06	12
						357	ND	ND	ND
						360	2.50E-02	2.60E+06	9.4
364	3.00E-02					3.20E+06	9.4		
367*	1.90E-02					4.40E+05	42		
369	3.10E-02					1.10E+06	27		
373*	2.60E-02					2.40E+05	110		
383	6.10E-02					1.70E+06	37		
413	2.20E-02					1.50E+06	14		
441	2.60E-02					3.60E+06	7.3		
448	2.70E-02					2.60E+06	11		
450	2.60E-02					3.60E+06	7.1		
458	3.20E-02					2.80E+06	12		
481	2.60E-02					3.70E+06	7.1		
516	5.50E-02					2.70E+06	20		
517	2.40E-02					2.80E+06	8.5		
518	1.70E-01					1.50E+07	0		
519	2.10E-02					3.70E+06	5.6		
520	2.40E-03					7.70E+05	3.1		
521	ND					ND	ND		
F	EY6A					RBD	4.80E-03	6.80E+05	7
						337	4.20E-03	8.20E+05	5.2
						344	3.40E-03	3.30E+05	10
						354	6.60E-03	4.00E+05	16
						357	5.00E-03	9.40E+05	5.3
						360	4.50E-03	4.60E+05	9.8
		364	2.20E-03			1.10E+06	2		
		367*	4.40E-03			2.10E+05	21		
		369	1.00E-02			3.80E+05	27		
		373*	4.10E-03			2.00E+05	21		
		383	ND			ND	ND		
		413	ND			ND	ND		
		441	4.80E-03			3.60E+05	13		
		448	4.90E-03			1.10E+06	4.5		
		450	4.50E-03			3.60E+05	13		
		458	5.40E-03			1.20E+06	4.6		
		481	4.90E-03			4.40E+05	11		
		516	3.70E-03			1.10E+06	3.4		
		517	7.90E-03			4.00E+05	20		
		518	5.20E-03			8.70E+05	6		
		519	4.10E-03			4.60E+05	9		
		520	5.20E-03			7.80E+05	6.6		
		521	ND			ND	ND		

*run in a different experiment, KD for RBD >2x higher than original experiment
 NT=not tested
 ND=poor fit, KD not determined
 For Koff/Kon rates outside the detectable range, the limits of the instrument were used to calculate the corrected KD

754

755

756 **References**

- 757 1. Dong, E., H. Du, and L. Gardner, *An interactive web-based dashboard to track COVID-19*
758 *in real time*. Lancet Infect Dis, 2020. **20**(5): p. 533-534.
- 759 2. Elbe, S. and G. Buckland-Merrett, *Data, disease and diplomacy: GISAID's innovative*
760 *contribution to global health*. Glob Chall, 2017. **1**(1): p. 33-46.
- 761 3. Letko, M., A. Marzi, and V. Munster, *Functional assessment of cell entry and receptor*
762 *usage for SARS-CoV-2 and other lineage B betacoronaviruses*. Nat Microbiol, 2020. **5**(4):
763 p. 562-569.
- 764 4. Zhou, P., et al., *A pneumonia outbreak associated with a new coronavirus of probable*
765 *bat origin*. Nature, 2020. **579**(7798): p. 270-273.
- 766 5. Wajnberg, A., et al., *Robust neutralizing antibodies to SARS-CoV-2 infection persist for*
767 *months*. Science, 2020. **370**(6521): p. 1227-1230.
- 768 6. Piccoli, L., et al., *Mapping Neutralizing and Immunodominant Sites on the SARS-CoV-2*
769 *Spike Receptor-Binding Domain by Structure-Guided High-Resolution Serology*. Cell,
770 2020. **183**(4): p. 1024-1042 e21.
- 771 7. Byrnes, J.R., et al., *Competitive SARS-CoV-2 Serology Reveals Most Antibodies Targeting*
772 *the Spike Receptor-Binding Domain Compete for ACE2 Binding*. mSphere, 2020. **5**(5).
- 773 8. Suthar, M.S., et al., *Rapid Generation of Neutralizing Antibody Responses in COVID-19*
774 *Patients*. Cell Rep Med, 2020. **1**(3): p. 100040.
- 775 9. Wang, L., et al., *Evaluation of candidate vaccine approaches for MERS-CoV*. Nat
776 Commun, 2015. **6**: p. 7712.
- 777 10. Yuan, M., et al., *Recognition of the SARS-CoV-2 receptor binding domain by neutralizing*
778 *antibodies*. Biochem Biophys Res Commun, 2020.
- 779 11. Raybould, M.I.J., et al., *CoV-AbDab: the Coronavirus Antibody Database*. Bioinformatics,
780 2020.
- 781 12. Brouwer, P.J.M., et al., *Potent neutralizing antibodies from COVID-19 patients define*
782 *multiple targets of vulnerability*. Science, 2020. **369**(6504): p. 643-650.
- 783 13. Ju, B., et al., *Human neutralizing antibodies elicited by SARS-CoV-2 infection*. Nature,
784 2020. **584**(7819): p. 115-119.
- 785 14. Liu, L., et al., *Potent neutralizing antibodies against multiple epitopes on SARS-CoV-2*
786 *spike*. Nature, 2020. **584**(7821): p. 450-456.
- 787 15. Rogers, T.F., et al., *Isolation of potent SARS-CoV-2 neutralizing antibodies and protection*
788 *from disease in a small animal model*. Science, 2020. **369**(6506): p. 956-963.
- 789 16. Wu, F.W., A.; Liu, M.; Wang, Q.; Chen, J.; Xia, S.; Ling, Y.; Zhang, Y.; Xun, J.; Lu, L.; Jiang,
790 S.; Lu, H.; Wen, Y.; Huang, J.. *Neutralizing antibody responses to SARS-CoV-2 in a COVID-*
791 *19 recovered patient cohort and their implications* medRxiv, 2020.
- 792 17. Yazici, M.K., et al., *Discordance between Serum Neutralizing Antibody Titers and the*
793 *Recovery from COVID-19*. Journal of Immunology, 2020. **205**(10): p. 2719-2725.
- 794 18. Lee, W.S., et al., *Antibody-dependent enhancement and SARS-CoV-2 vaccines and*
795 *therapies*. Nat Microbiol, 2020. **5**(10): p. 1185-1191.

- 796 19. de Taeye, S.W., et al., *Stabilization of the gp120 V3 loop through hydrophobic*
797 *interactions reduces the immunodominant V3-directed non-neutralizing response to HIV-*
798 *1 envelope trimers*. J Biol Chem, 2018. **293**(5): p. 1688-1701.
- 799 20. Kulp, D.W., et al., *Structure-based design of native-like HIV-1 envelope trimers to silence*
800 *non-neutralizing epitopes and eliminate CD4 binding*. Nat Commun, 2017. **8**(1): p. 1655.
- 801 21. Sanders, R.W., et al., *A next-generation cleaved, soluble HIV-1 Env trimer, BG505*
802 *SOSIP.664 gp140, expresses multiple epitopes for broadly neutralizing but not non-*
803 *neutralizing antibodies*. PLoS Pathog, 2013. **9**(9): p. e1003618.
- 804 22. Ren, H. and P. Zhou, *Epitope-focused vaccine design against influenza A and B viruses*.
805 Curr Opin Immunol, 2016. **42**: p. 83-90.
- 806 23. Impagliazzo, A., et al., *A stable trimeric influenza hemagglutinin stem as a broadly*
807 *protective immunogen*. Science, 2015. **349**(6254): p. 1301-6.
- 808 24. Krammer, F. and P. Palese, *Influenza virus hemagglutinin stalk-based antibodies and*
809 *vaccines*. Curr Opin Virol, 2013. **3**(5): p. 521-30.
- 810 25. Yassine, H.M., et al., *Hemagglutinin-stem nanoparticles generate heterosubtypic*
811 *influenza protection*. Nat Med, 2015. **21**(9): p. 1065-70.
- 812 26. Du, L., et al., *Introduction of neutralizing immunogenicity index to the rational design of*
813 *MERS coronavirus subunit vaccines*. Nat Commun, 2016. **7**: p. 13473.
- 814 27. Barnes, C.O., et al., *SARS-CoV-2 neutralizing antibody structures inform therapeutic*
815 *strategies*. Nature, 2020. **588**(7839): p. 682-687.
- 816 28. Wu, N.C., et al., *An Alternative Binding Mode of IGHV3-53 Antibodies to the SARS-CoV-2*
817 *Receptor Binding Domain*. Cell Rep, 2020. **33**(3): p. 108274.
- 818 29. Watanabe, Y., et al., *Exploitation of glycosylation in enveloped virus pathobiology*.
819 Biochim Biophys Acta Gen Subj, 2019. **1863**(10): p. 1480-1497.
- 820 30. Hariharan, V. and R.S. Kane, *Glycosylation as a tool for rational vaccine design*.
821 Biotechnol Bioeng, 2020. **117**(8): p. 2556-2570.
- 822 31. Ly, A. and L. Stamatatos, *V2 loop glycosylation of the human immunodeficiency virus*
823 *type 1 SF162 envelope facilitates interaction of this protein with CD4 and CCR5 receptors*
824 *and protects the virus from neutralization by anti-V3 loop and anti-CD4 binding site*
825 *antibodies*. J Virol, 2000. **74**(15): p. 6769-76.
- 826 32. Medina, R.A., et al., *Glycosylations in the globular head of the hemagglutinin protein*
827 *modulate the virulence and antigenic properties of the H1N1 influenza viruses*. Sci Transl
828 Med, 2013. **5**(187): p. 187ra70.
- 829 33. Wanzeck, K., K.L. Boyd, and J.A. McCullers, *Glycan shielding of the influenza virus*
830 *hemagglutinin contributes to immunopathology in mice*. Am J Respir Crit Care Med,
831 2011. **183**(6): p. 767-73.
- 832 34. Wei, X., et al., *Antibody neutralization and escape by HIV-1*. Nature, 2003. **422**(6929): p.
833 307-12.
- 834 35. Bajic, G., et al., *Influenza Antigen Engineering Focuses Immune Responses to a*
835 *Subdominant but Broadly Protective Viral Epitope*. Cell Host Microbe, 2019. **25**(6): p.
836 827-835 e6.
- 837 36. Ingale, J., et al., *Hyperglycosylated stable core immunogens designed to present the CD4*
838 *binding site are preferentially recognized by broadly neutralizing antibodies*. J Virol,
839 2014. **88**(24): p. 14002-16.

- 840 37. Xu, Z., et al., *A DNA-Launched Nanoparticle Vaccine Elicits CD8(+) T-cell Immunity to*
841 *Promote In Vivo Tumor Control*. *Cancer Immunol Res*, 2020. **8**(11): p. 1354-1364.
- 842 38. Xu, Z., et al., *In Vivo Assembly of Nanoparticles Achieved through Synergy of Structure-*
843 *Based Protein Engineering and Synthetic DNA Generates Enhanced Adaptive Immunity*.
844 *Adv Sci (Weinh)*, 2020. **7**(8): p. 1902802.
- 845 39. Manolova, V., et al., *Nanoparticles target distinct dendritic cell populations according to*
846 *their size*. *Eur J Immunol*, 2008. **38**(5): p. 1404-13.
- 847 40. Kelly, H.G., S.J. Kent, and A.K. Wheatley, *Immunological basis for enhanced immunity of*
848 *nanoparticle vaccines*. *Expert Rev Vaccines*, 2019. **18**(3): p. 269-280.
- 849 41. Smith, T.R.F., et al., *Immunogenicity of a DNA vaccine candidate for COVID-19*. *Nat*
850 *Commun*, 2020. **11**(1): p. 2601.
- 851 42. Huo, J., et al., *Neutralization of SARS-CoV-2 by Destruction of the Prefusion Spike*. *Cell*
852 *Host Microbe*, 2020. **28**(3): p. 497.
- 853 43. Yuan, M., et al., *A highly conserved cryptic epitope in the receptor binding domains of*
854 *SARS-CoV-2 and SARS-CoV*. *Science*, 2020. **368**(6491): p. 630-633.
- 855 44. Zhou, D., et al., *Structural basis for the neutralization of SARS-CoV-2 by an antibody from*
856 *a convalescent patient*. *Nat Struct Mol Biol*, 2020. **27**(10): p. 950-958.
- 857 45. Seydoux, E., et al., *Analysis of a SARS-CoV-2-Infected Individual Reveals Development of*
858 *Potent Neutralizing Antibodies with Limited Somatic Mutation*. *Immunity*, 2020. **53**(1): p.
859 98-105 e5.
- 860 46. Hansen, J., et al., *Studies in humanized mice and convalescent humans yield a SARS-CoV-*
861 *2 antibody cocktail*. *Science*, 2020. **369**(6506): p. 1010-1014.
- 862 47. Wu, Y., et al., *A noncompeting pair of human neutralizing antibodies block COVID-19*
863 *virus binding to its receptor ACE2*. *Science*, 2020. **368**(6496): p. 1274-1278.
- 864 48. Shi, R., et al., *A human neutralizing antibody targets the receptor-binding site of SARS-*
865 *CoV-2*. *Nature*, 2020. **584**(7819): p. 120-124.
- 866 49. Pinto, D., et al., *Cross-neutralization of SARS-CoV-2 by a human monoclonal SARS-CoV*
867 *antibody*. *Nature*, 2020. **583**(7815): p. 290-295.
- 868 50. Robbiani, D.F., et al., *Convergent antibody responses to SARS-CoV-2 in convalescent*
869 *individuals*. *Nature*, 2020. **584**(7821): p. 437-442.
- 870 51. Tian, X., et al., *Potent binding of 2019 novel coronavirus spike protein by a SARS*
871 *coronavirus-specific human monoclonal antibody*. *Emerg Microbes Infect*, 2020. **9**(1): p.
872 382-385.
- 873 52. Walker, S.N., et al., *SARS-CoV-2 Assays To Detect Functional Antibody Responses That*
874 *Block ACE2 Recognition in Vaccinated Animals and Infected Patients*. *J Clin Microbiol*,
875 2020. **58**(11).
- 876 53. Zhao, L., et al., *Nanoparticle vaccines*. *Vaccine*, 2014. **32**(3): p. 327-37.
- 877 54. Xu, Z., et al., *Incorporation of a Novel CD4+ Helper Epitope Identified from Aquifex*
878 *aeolicus Enhances Humoral Responses Induced by DNA and Protein Vaccinations*.
879 *iScience*, 2020. **23**(8): p. 101399.
- 880 55. Dai, L., et al., *A Universal Design of Betacoronavirus Vaccines against COVID-19, MERS,*
881 *and SARS*. *Cell*, 2020. **182**(3): p. 722-733 e11.

- 882 56. Chow, Y.H., et al., *Development of an epithelium-specific expression cassette with*
883 *human DNA regulatory elements for transgene expression in lung airways.* Proc Natl
884 Acad Sci U S A, 1997. **94**(26): p. 14695-700.
- 885 57. McCray, P.B., Jr., et al., *Lethal infection of K18-hACE2 mice infected with severe acute*
886 *respiratory syndrome coronavirus.* J Virol, 2007. **81**(2): p. 813-21.
- 887 58. Oladunni, F.S., et al., *Lethality of SARS-CoV-2 infection in K18 human angiotensin-*
888 *converting enzyme 2 transgenic mice.* Nat Commun, 2020. **11**(1): p. 6122.
- 889 59. Rathnasinghe, R., et al., *Comparison of transgenic and adenovirus hACE2 mouse models*
890 *for SARS-CoV-2 infection.* Emerg Microbes Infect, 2020. **9**(1): p. 2433-2445.
- 891 60. Geurts, A.M., et al., *Knockout rats via embryo microinjection of zinc-finger nucleases.*
892 Science, 2009. **325**(5939): p. 433.
- 893 61. Altman, M.O., et al., *Human Influenza A Virus Hemagglutinin Glycan Evolution Follows a*
894 *Temporal Pattern to a Glycan Limit.* mBio, 2019. **10**(2).
- 895 62. Gary, E.N. and D.B. Weiner, *DNA vaccines: prime time is now.* Curr Opin Immunol, 2020.
896 **65**: p. 21-27.
- 897 63. Polack, F.P., et al., *Safety and Efficacy of the BNT162b2 mRNA Covid-19 Vaccine.* N Engl J
898 Med, 2020. **383**(27): p. 2603-2615.
- 899 64. Baden, L.R., et al., *Efficacy and Safety of the mRNA-1273 SARS-CoV-2 Vaccine.* N Engl J
900 Med, 2021. **384**(5): p. 403-416.
- 901 65. Yu, J., et al., *DNA vaccine protection against SARS-CoV-2 in rhesus macaques.* Science,
902 2020. **369**(6505): p. 806-811.
- 903 66. Brouwer, P.J.M., et al., *Two-component spike nanoparticle vaccine protects macaques*
904 *from SARS-CoV-2 infection.* Cell, 2021. **184**(5): p. 1188-1200 e19.
- 905 67. Walls, A.C., et al., *Elicitation of Potent Neutralizing Antibody Responses by Designed*
906 *Protein Nanoparticle Vaccines for SARS-CoV-2.* Cell, 2020. **183**(5): p. 1367-1382 e17.
- 907 68. Cohen, A.A., et al., *Mosaic nanoparticles elicit cross-reactive immune responses to*
908 *zoonotic coronaviruses in mice.* Science, 2021. **371**(6530): p. 735-741.
- 909 69. He, L., et al., *Self-assembling nanoparticles presenting receptor binding domain and*
910 *stabilized spike as next-generation COVID-19 vaccines.* bioRxiv, 2020.
- 911 70. Zhang, B., et al., *A platform incorporating trimeric antigens into self-assembling*
912 *nanoparticles reveals SARS-CoV-2-spike nanoparticles to elicit substantially higher*
913 *neutralizing responses than spike alone.* Sci Rep, 2020. **10**(1): p. 18149.
- 914 71. Tan, T.K., et al., *A COVID-19 vaccine candidate using SpyCatcher multimerization of the*
915 *SARS-CoV-2 spike protein receptor-binding domain induces potent neutralising antibody*
916 *responses.* Nat Commun, 2021. **12**(1): p. 542.
- 917 72. Ma, X., et al., *Nanoparticle Vaccines Based on the Receptor Binding Domain (RBD) and*
918 *Heptad Repeat (HR) of SARS-CoV-2 Elicit Robust Protective Immune Responses.*
919 Immunity, 2020. **53**(6): p. 1315-1330 e9.
- 920 73. Lei, C., et al., *On the Calculation of TCID50 for Quantitation of Virus Infectivity.* Virol Sin,
921 2021. **36**(1): p. 141-144.
- 922 74. Scheres, S.H., *A Bayesian view on cryo-EM structure determination.* J Mol Biol, 2012.
923 **415**(2): p. 406-18.
- 924 75. Rohou, A. and N. Grigorieff, *CTFFIND4: Fast and accurate defocus estimation from*
925 *electron micrographs.* J Struct Biol, 2015. **192**(2): p. 216-21.

